

# A Unified Framework for Dynamic Analysis of Tensegrity Structures with Arbitrary Rigid Bodies and Rigid Bars

Jiahui Luo<sup>a</sup>, Zhigang Wu<sup>a</sup>, Xiaoming Xu<sup>a,b,\*</sup>

<sup>a</sup> School of Aeronautics and Astronautics, Sun Yat-sen University, No.66 Gongchang Road, Guangming District, Shenzhen, 518107, China

<sup>b</sup> State Key Laboratory of Structural Analysis for Industrial Equipment, Dalian University of Technology, No.2 Linggong Road, Ganjingzi District, Dalian, 116024, China

---

## Abstract

This paper develops a unified framework to study the dynamics of tensegrity systems with any arbitrary rigid bodies and rigid bars. The natural coordinates are adopted as a completely non-minimal modeling approach to describe both rigid bodies and rigid bars in terms of different combinations of basic points and base vectors. Various coordinate combinations are then unified into polymorphic expressions that succinctly encompass Class-1-to- $k$  tensegrities. Then, the Lagrange-d'Alembert principle is employed to derive the dynamic equation, which has a constant mass matrix and is free from trigonometric functions as well as centrifugal and Coriolis terms. For numerical analysis of nonlinear dynamics, a modified symplectic integration scheme is derived, accommodating non-conservative forces and boundary conditions. Additionally, formulations for statics and linearized dynamics around static equilibrium states are derived to help determine cable actuation values and calculate natural frequencies and mode shapes, which are commonly needed for structural analyses. Numerical examples are given to demonstrate the proposed approach's abilities in modeling tensegrity structures composed of Class-1-to- $k$  modules and conducting dynamic simulations with complex conditions, including slack cables, gravity loads, seismic grounds, and cable-based deployments. Finally, two novel designs of tensegrity structures exemplify new ways to create multi-functional composite structures.

**Keywords:** tensegrity, dynamic modeling, natural coordinates, modal analysis, symplectic integration

---

## 1. Introduction

The term *tensegrity*, combining “tensile” and “integrity”, was coined by Buckminster Fuller [1] to describe a kind of prestressed structures, that were created by Ioganson and Snelson [2]. A commonly adopted definition is given by [3]: a tensegrity structure is a self-sustaining composition of rigid members and tensile members, and if there is at least a torqueless joint connecting  $k$  rigid members, it is called a Class- $k$  tensegrity. Recent decades have witnessed two trends of developments in the tensegrity literature.

One trend is interested in a subset of tensegrity structures, where the rigid members are thin bars and are connected to cables only via their endpoints. Because this setting makes all members axial-loaded, i.e. in either tension or compression, material efficiency can be maximized. Consequently, these “bars-only” tensegrities are inherently strong and lightweight with the potential for minimal mass designs [3]. Mathematical elegance is also recognized, because both compressive and tensile members can be treated as the same elements, differing only in the signs of their force densities. Furthermore, many “bars-only” tensegrities are found to be deployable using simple cable-based actuations [4–6]. Thus, this trend of development is mostly seen in civil engineering [7–9] and aerospace [10–12], etc. However, “bars-only” tensegrities are not without their problems: they usually have numerous bars and cables making them hard to fabricate and assemble; they have little capacity space for attachments; and

the interfaces between different modules are complicated.

The other trend concerns tensegrities with rigid bodies, which are allowed to have complex shapes instead of being thin bars only. Tensegrities with rigid bodies can date back to the “X-Piece” (one of the earliest tensegrities created by Snelson [13]). Compared to the “bars-only” setting, they usually have fewer members and larger capacity spaces for attachments, while still being modular and compliant. Furthermore, they are recognized in biology to explain structural properties such as the interactions of muscles and bones [3, 7], and the integrity of vertebrate spines [14]. Thus, they are often used in the robotics literature to create bio-inspired designs, such as tensegrity joints [15] and tensegrity fishes [16], etc.

The interest in merging these two trends has been growing in recent years. For instance, Ref. [17] proposes a novel tensegrity robotic unit which combines a rigid triangular frame and a rigid bar to simplify topology. Ref. [18] devises a topology-finding method to discover new structures like the tensegrity bridge, which has not only bars as supporting struts but also a rigid plate as the bridge deck. The motivation to integrate rigid bodies and rigid bars into one tensegrity structure is the possibility to make their respective advantages complementary to each other. On the one hand, the rigid bars, when connected with cables, can provide high-strength-low-weight support and deployability. On the other hand, the rigid bodies in a tensegrity help simplify the interfaces between different modules, hold actuators and payloads, and provide a certain degree of biomimetic functionalities.

Consequently, a unified framework for dynamic analysis of tensegrity structures including both arbitrary rigid bodies and rigid bars is called for. However,

---

\*Corresponding author

Email addresses: luojiah3@mail2.sysu.edu.cn (Jiahui Luo), wuzhigang@mail.sysu.edu.cn (Zhigang Wu), xuxm29@mail.sysu.edu.cn (Xiaoming Xu)

this “bodies-and-bars” setting presents difficulties due to the differences between them in 3D space. First, the vanishing inertia about the longitudinal axis of a thin bar can lead to singular mass matrices [19]. Therefore, this thin-bar assumption is often relaxed to give some thickness to them, so that rigid body dynamics can be applied [20, 21]. Nonetheless, the rotation and angular velocity about the axis of a bar, either thin or thick, are still ill-defined. In other words, a 3D rigid bar has only five degrees of freedom (DoFs), one less than a 6-DoF 3D rigid body. Therefore, special treatments may be needed to determine the orientation parameters [22].

For “bars-only” tensegrities, a series of works [23–28] develop specialized non-minimal formulations which use the nodal coordinates of two endpoints and a bar length constraint, i.e. six coordinates and one constraint, to uniquely define the dynamics of a 3D rigid bar, and thereby resolve those difficulties. Additionally, the non-minimal formulations are found to have other nice properties for dynamic analyses: the mass matrix is constant; inertia quadratic velocity terms for centrifugal forces and Coriolis forces vanish; and no trigonometric function is involved.

Therefore, in the “bodies-and-bars” setting of tensegrity structures, it would be beneficial to retain the non-minimal formulations of rigid bars. In line with this thought, a recent work [29] combines the nodal coordinates of rigid bars and minimal coordinates of rigid bodies to formulate static equilibrium equations for form-finding problems. However, it has not developed dynamic equations, and the introduction of minimal coordinates can have “contaminating” effects on the formulations. For example, Euler angles are used as a minimal description of orientations [29], so trigonometric functions are unavoidable.

In this paper, we develop a unified framework for dynamic analysis of tensegrity structures, where not only rigid bars but also arbitrary rigid bodies are described by non-minimal formulations through the natural coordinates [30–33]. In this way, the notable features of non-minimal formulations are preserved. Furthermore, the natural coordinates are comprehensively reformed better to suit the needs in the modeling of tensegrity structures. First, different types of coordinate combinations are exhaustingly derived for arranging basic points and base vectors on 3D and 2D rigid bodies. This helps to reduce the number of coordinates and gives analysts more flexibility to model torqueless joints which are present in Class- $k$  ( $k > 1$ ) tensegrity structures. Second, by the use of polymorphism and conversions between the different types of coordinate combinations, the formulations of both rigid bodies and rigid bars in both 3D and 2D spaces are unified. This helps to write succinct mathematical expressions and is beneficial to implement generic computer codes. Third, a coordinate-separating strategy is employed to deal with fixed and moving boundary conditions. Fourth, explicit formulations of cables’ tension forces reveal the linear dependence of the system’s dynamics on the force densities, potentially helpful for structural control.

Additionally, solution methods for static and dynamic analyses are derived. First, forward and inverse static analysis formulations are derived for the ease of complete analyses in the same framework. Second, linearized dynamics is derived to allow for modal analyses to calculate natural frequencies and

mode shapes. Third, numerical analysis of nonlinear dynamics is enabled by a symplectic integration scheme, which is modified to accommodate non-conservative forces as well as fixed and moving boundary conditions.

Finally, two new tensegrity structures are studied to verify the proposed approach and to demonstrate the innovative possibilities of integrating rigid bodies and rigid bars into one tensegrity system.

The rest of this paper is organized as follows. Sec. 2 derives the unifying formulations for 3D and 2D rigid bodies and rigid bars, based on which Sec. 3 model the tensegrity structures. Secs. 4 and 5 derives solution methods for static and dynamic problems, respectively, followed by the numerical examples in Sec. 6. Finally, conclusions are drawn in Sec. 7.

## 2. Unifying rigid bodies and rigid bars using natural coordinates

In this section, the natural coordinates [34, 35] are adapted for unifying the non-minimal descriptions of rigid bodies and rigid bars, which are collectively called rigid members, and indistinguishably labeled by circled numbers ①, ②, . . . , or circled capital letters ①, ②, . . . , etc. Thus, a quantity with a capital subscript, such as  $(\cdot)_I$ , indicates the quantity belongs to the  $I$ th rigid member.

### 2.1. Rigid bodies of arbitrary shapes

#### 2.1.1. 3D rigid bodies

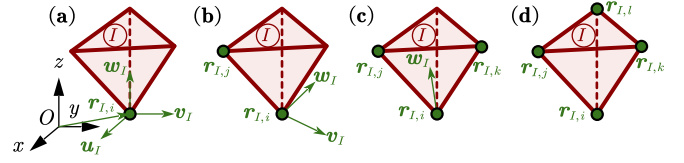


Figure 1: A 3D rigid body described by the (a) RUVW, (b) RRVW, (c) RRRW, and (d) RRRR type natural coordinates. Rigid bodies are drawn by red lines. Basic points and base vectors are colored in green.

Consider a tetrahedron which exemplifies an arbitrary 3D rigid body, as shown in Fig. 1, where basic points  $\mathbf{r}_{I,i}, \mathbf{r}_{I,j}, \mathbf{r}_{I,k}, \mathbf{r}_{I,l} \in \mathbb{R}^3$  and base vectors  $\mathbf{u}_I, \mathbf{v}_I, \mathbf{w}_I \in \mathbb{R}^3$  are fixed on the rigid body and expressed in the global inertial frame  $Oxyz$ . Four types of natural coordinates, i.e.

$$\begin{aligned} \mathbf{q}_{I,\text{ruvw}} &= [\mathbf{r}_{I,i}^T, \mathbf{u}_I^T, \mathbf{v}_I^T, \mathbf{w}_I^T]^T, & \mathbf{q}_{I,\text{rrvw}} &= [\mathbf{r}_{I,i}^T, \mathbf{r}_{I,j}^T, \mathbf{v}_I^T, \mathbf{w}_I^T]^T, \\ \mathbf{q}_{I,\text{rrrw}} &= [\mathbf{r}_{I,i}^T, \mathbf{r}_{I,j}^T, \mathbf{r}_{I,k}^T, \mathbf{w}_I^T]^T, & \text{and } \mathbf{q}_{I,\text{rrrr}} &= [\mathbf{r}_{I,i}^T, \mathbf{r}_{I,j}^T, \mathbf{r}_{I,k}^T, \mathbf{r}_{I,l}^T]^T \in \mathbb{R}^{12}, \end{aligned} \quad (1)$$

can be used to describe a 3D rigid body, corresponding to Fig. 1(a) to (d), respectively, where  $(\cdot)_{\text{ruvw}}$ , etc, denote the type of natural coordinates. For the latter three types of natural coordinates, we can formally define  $\mathbf{u}_I = \mathbf{r}_{I,j} - \mathbf{r}_{I,i}$ ,  $\mathbf{v}_I = \mathbf{r}_{I,k} - \mathbf{r}_{I,i}$ , and  $\mathbf{w}_I = \mathbf{r}_{I,l} - \mathbf{r}_{I,i}$ , so that they can be converted to the first type by

$$\mathbf{q}_{I,\text{ruvw}} = \mathbf{Y}_{\text{rrvw}} \mathbf{q}_{I,\text{rrvw}} = \mathbf{Y}_{\text{rrrw}} \mathbf{q}_{I,\text{rrrw}} = \mathbf{Y}_{\text{rrrr}} \mathbf{q}_{I,\text{rrrr}}, \quad (2)$$

where the conversion matrices are defined as, respectively,

$$\mathbf{Y}_{\text{rrvw}} = \begin{bmatrix} 1 & 0 & 0 & 0 \\ -1 & 1 & 0 & 0 \\ 0 & 0 & 1 & 0 \\ 0 & 0 & 0 & 1 \end{bmatrix} \otimes \mathbf{I}_3, \quad \mathbf{Y}_{\text{rrrw}} = \begin{bmatrix} 1 & 0 & 0 & 0 \\ -1 & 1 & 0 & 0 \\ -1 & 0 & 1 & 0 \\ 0 & 0 & 0 & 1 \end{bmatrix} \otimes \mathbf{I}_3, \quad \text{and } \mathbf{Y}_{\text{rrrr}} = \begin{bmatrix} 1 & 0 & 0 & 0 \\ -1 & 1 & 0 & 0 \\ -1 & 0 & 1 & 0 \\ -1 & 0 & 0 & 1 \end{bmatrix} \otimes \mathbf{I}_3 \quad (3)$$

where  $\mathbf{I}_3$  is a  $3 \times 3$  identity matrix, and  $\otimes$  denotes the Kronecker product.

Note that the base vectors are assumed to be non-coplanar, thus the natural coordinates actually form an affine frame attached to the 3D rigid body. Consequently, the position vector of a generic point on the 3D rigid body can be expressed by

$$\mathbf{r} = \mathbf{r}_{I,i} + c_{I,1}\mathbf{u}_I + c_{I,2}\mathbf{v}_I + c_{I,3}\mathbf{w}_I = \mathbf{C}_{I,\text{ruvw}}\mathbf{q}_{I,\text{ruvw}}, \quad (4)$$

where  $c_{I,1}$ ,  $c_{I,2}$  and  $c_{I,3}$  are the coordinates of the generic point in the affine frame, and  $\mathbf{C}_{I,\text{ruvw}} = [1, c_{I,1}, c_{I,2}, c_{I,3}] \otimes \mathbf{I}_3$  is a transformation matrix for  $\mathbf{q}_{I,\text{ruvw}}$ .

To ensure rigidity of the body, the natural coordinates  $\mathbf{q}_{I,\text{ruvw}}$  must satisfy six intrinsic constraints

$$\Phi_I(\mathbf{q}_{I,\text{ruvw}}) = \begin{pmatrix} \mathbf{u}_I^T \mathbf{u}_I - \bar{\mathbf{u}}_I^T \bar{\mathbf{u}}_I \\ \mathbf{v}_I^T \mathbf{v}_I - \bar{\mathbf{v}}_I^T \bar{\mathbf{v}}_I \\ \mathbf{w}_I^T \mathbf{w}_I - \bar{\mathbf{w}}_I^T \bar{\mathbf{w}}_I \\ \mathbf{v}_I^T \mathbf{w}_I - \bar{\mathbf{v}}_I^T \bar{\mathbf{w}}_I \\ \mathbf{u}_I^T \mathbf{w}_I - \bar{\mathbf{u}}_I^T \bar{\mathbf{w}}_I \\ \mathbf{u}_I^T \mathbf{v}_I - \bar{\mathbf{u}}_I^T \bar{\mathbf{v}}_I \end{pmatrix} = \mathbf{0} \quad (5)$$

where  $\bar{\mathbf{u}}_I$ ,  $\bar{\mathbf{v}}_I$  and  $\bar{\mathbf{w}}_I$  are constant vectors in a local frame, which is fixed on the rigid member (See also Appendix A). Then, the position and orientation of a 6-DoF 3D rigid body can be defined by twelve coordinates (any type in (1)) and six constraints (5).

### 2.1.2. 2D rigid bodies

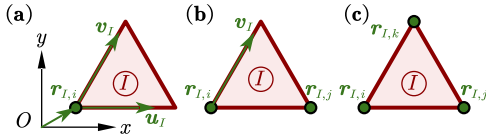


Figure 2: A 2D rigid body described by the (a) RUV, (b) RRV, and (c) RRR type natural coordinates.

Natural coordinates for a 2D rigid body are developed in the same vein as for the 3D case. Three types of natural coordinates,

$$\mathbf{q}_{I,\text{ruv}} = [\mathbf{r}_{I,i}^T, \mathbf{u}_I^T, \mathbf{v}_I^T]^T, \mathbf{q}_{I,\text{rvv}} = [\mathbf{r}_{I,i}^T, \mathbf{r}_{I,j}^T, \mathbf{v}_I^T]^T, \quad \text{and} \quad (6)$$

$$\mathbf{q}_{I,\text{rrr}} = [\mathbf{r}_{I,i}^T, \mathbf{r}_{I,j}^T, \mathbf{r}_{I,k}^T]^T \in \mathbb{R}^6$$

corresponding to Fig. 2(a) to (c), respectively, are available for a 2D rigid body.

The latter two types can be converted to the first type by

$$\mathbf{q}_{I,\text{ruv}} = \mathbf{Y}_{\text{rvv}}\mathbf{q}_{I,\text{rvv}} = \mathbf{Y}_{\text{rrr}}\mathbf{q}_{I,\text{rrr}} \quad (7)$$

with

$$\mathbf{Y}_{\text{rvv}} = \begin{bmatrix} 1 & 0 & 0 \\ -1 & 1 & 0 \\ 0 & 0 & 1 \end{bmatrix} \otimes \mathbf{I}_2 \quad \text{and} \quad \mathbf{Y}_{\text{rrr}} = \begin{bmatrix} 1 & 0 & 0 \\ -1 & 1 & 0 \\ -1 & 0 & 1 \end{bmatrix} \otimes \mathbf{I}_2. \quad (8)$$

The base vectors are assumed to be non-collinear. So the position vector of a generic point on the 2D rigid body can be expressed by

$$\mathbf{r} = \mathbf{r}_{I,i} + c_{I,1}\mathbf{u}_I + c_{I,2}\mathbf{v}_I = \mathbf{C}_{I,\text{ruv}}\mathbf{q}_{I,\text{ruv}} \quad (9)$$

where  $c_{I,1}$  and  $c_{I,2}$  are the coordinates of the generic point in the affine frame formed by the basic points and base vectors, and  $\mathbf{C}_{I,\text{ruv}} = [1, c_{I,1}, c_{I,2}] \otimes \mathbf{I}_2$  is the transformation matrix for  $\mathbf{q}_{I,\text{ruv}}$ .

And the three intrinsic constraints that ensure the rigidity are

$$\Phi_I(\mathbf{q}_{I,\text{ruv}}) = \begin{pmatrix} \mathbf{u}_I^T \mathbf{u}_I - \bar{\mathbf{u}}_I^T \bar{\mathbf{u}}_I \\ \mathbf{v}_I^T \mathbf{v}_I - \bar{\mathbf{v}}_I^T \bar{\mathbf{v}}_I \\ \mathbf{u}_I^T \mathbf{v}_I - \bar{\mathbf{u}}_I^T \bar{\mathbf{v}}_I \end{pmatrix} = \mathbf{0} \quad (10)$$

Then, the position and orientation of a 3-DoF 2D rigid body can be defined by six coordinates (any type in (6)) and three constraints (10).

### 2.2. 3D and 2D rigid bars

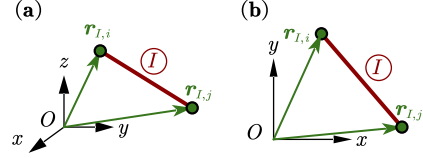


Figure 3: A (a) 3D or (b) 2D rigid bar described by the two basic points.

In either 3D or 2D space, as shown in Fig. 3(a) and (b), respectively, a rigid bar can be described by its two endpoints  $\mathbf{r}_{I,i}$  and  $\mathbf{r}_{I,j} \in \mathbb{R}^m$ , which are used as basic points to form the natural coordinates  $\mathbf{q}_{I,\text{rr}} = [\mathbf{r}_{I,i}^T, \mathbf{r}_{I,j}^T]^T \in \mathbb{R}^{2m}$ , where  $m$  denotes the space dimension. In order to have similar formulations as in Sec. 2.1, we convert  $\mathbf{q}_{I,\text{rr}}$  to the standard type  $\mathbf{q}_{I,\text{ru}} = [\mathbf{r}_I^T, \mathbf{u}_I^T]^T \in \mathbb{R}^{2m}$  by

$$\mathbf{q}_{I,\text{ru}} = \mathbf{Y}_{\text{rr}}\mathbf{q}_{I,\text{rr}} \quad \text{with} \quad \mathbf{Y}_{\text{rr}} = \begin{bmatrix} 1 & 0 \\ -1 & 1 \end{bmatrix} \otimes \mathbf{I}_m \quad (11)$$

The position vector of a generic point along the longitudinal axis of the rigid bar is given by

$$\mathbf{r} = \mathbf{r}_{I,i} + c_I \mathbf{u}_I = \mathbf{C}_{I,\text{ru}}\mathbf{q}_{I,\text{ru}} \quad (12)$$

where the coefficient  $c_I$  depends on the relative position of the generic point, and  $\mathbf{C}_{I,\text{ru}} = [1, c_I] \otimes \mathbf{I}_m$  is the transformation matrix for  $\mathbf{q}_{I,\text{ru}}$ .

And the intrinsic constraint to preserve the bar length is

$$\Phi_I(\mathbf{q}_{I,\text{ru}}) = \mathbf{u}_I^T \mathbf{u}_I - \bar{\mathbf{u}}_I^T \bar{\mathbf{u}}_I = 0 \quad (13)$$

Then, the position and orientation of a 5-DoF 3D (or 3-DoF 2D) rigid bar can be defined by six (or four) coordinates and one constraint (13).

### 2.3. Unified formulations and mass matrices

The transformation relations (4), (9), and (12) for the standard types of natural coordinates can be put into a unifying form

$$\mathbf{r} = \mathbf{C}_{I,\text{std}}\mathbf{q}_{I,\text{std}}, \quad (14)$$

where the subscript  $(\text{std})$  can be any of  $(\text{ruvw})$ ,  $(\text{ruv})$ , or  $(\text{ru})$ . And the transformation matrix is defined as  $\mathbf{C}_{I,\text{std}} = [1, \mathbf{c}_I^T] \otimes \mathbf{I}_m$ , where the length of  $\mathbf{c}_I$  is 1, 2, or 3.

Using linear conversions (2), (7), and (11), transformation relations for any nonstandard types of natural coordinates are unified by,

$$\mathbf{r} = \mathbf{C}_{I,\text{nonstd}}\mathbf{q}_{I,\text{nonstd}} \quad \text{with} \quad \mathbf{C}_{I,\text{nonstd}} = \mathbf{C}_{I,\text{std}}\mathbf{Y}_{\text{nonstd}} \quad (15)$$

Table 1: Polymorphism of natural coordinates for rigid bodies and rigid bars

		Rigid body		Rigid bar	
Dimension of space		3D	2D	3D	2D
Degrees of freedom		6	3	5	3
Number of coordinates		12	6	6	4
UNIFIED	STD	RUUVW	RUUV	RU	RU
	NONSTD	RRVW	RRV	RR	RR
		RRRW	RRR		
		RRRR			

For example, we have  $\mathbf{r} = \mathbf{C}_{I,\text{rrr}}\mathbf{q}_{I,\text{rrr}} = \mathbf{C}_{I,\text{ruvw}}\mathbf{q}_{I,\text{ruvw}}$ , so  $\mathbf{C}_{I,\text{rrr}} = \mathbf{C}_{I,\text{ruvw}}\mathbf{Y}_{\text{rrr}}$ .

Ultimately, (14) and (15) are unified by

$$\mathbf{r} = \mathbf{C}_I\mathbf{q}_I \quad (16)$$

which is a polymorphic expression. The polymorphism of natural coordinates is summarized in Tab. 1.

Note that while the specific expression of  $\mathbf{C}_I$  varies with  $\mathbf{q}_I$ , it is not a function of the latter. Consequently, the velocity of a generic point is given by  $\dot{\mathbf{r}} = \mathbf{C}_I\dot{\mathbf{q}}_I$ , which can be used to derive the mass matrix. Let  $\rho_I$  denote the linear, area, or volume density of the rigid member  $\mathcal{I}$ . Then, the kinetic energy can be computed by an integral over its entire domain  $\Omega$  as

$$T_I = \frac{1}{2} \int_{\Omega} \rho_I \dot{\mathbf{r}}^T \dot{\mathbf{r}} d\Omega = \frac{1}{2} \int_{\Omega} \rho_I \dot{\mathbf{q}}_I^T \mathbf{C}_I^T \mathbf{C}_I \dot{\mathbf{q}}_I d\Omega = \frac{1}{2} \dot{\mathbf{q}}_I^T \mathbf{M}_I \dot{\mathbf{q}}_I \quad (17)$$

where  $\mathbf{M}_I$  is a constant mass matrix with polymorphism defined by

$$\mathbf{M}_{I,\text{std}} = \int_{\Omega} \rho_I \mathbf{C}_I^T \mathbf{C}_I d\Omega = \int_{\Omega} \left( \rho_I \begin{bmatrix} 1 & \mathbf{c}_I^T \\ \mathbf{c}_I & \mathbf{c}_I \mathbf{c}_I^T \end{bmatrix} \right) d\Omega \otimes \mathbf{I}_m \quad (18a)$$

$$= \begin{bmatrix} \int_{\Omega} \rho_I d\Omega & \int_{\Omega} \rho_I \mathbf{c}_I^T d\Omega \\ \int_{\Omega} \rho_I \mathbf{c}_I d\Omega & \int_{\Omega} \rho_I \mathbf{c}_I \mathbf{c}_I^T d\Omega \end{bmatrix} \otimes \mathbf{I}_m \quad (18b)$$

$$\mathbf{M}_{I,\text{nonstd}} = \mathbf{Y}_{\text{nonstd}}^T \mathbf{M}_{I,\text{std}} \mathbf{Y}_{\text{nonstd}} \quad (18c)$$

It is possible to express the mass matrix by conventional inertia properties, such as the mass, the center of mass, and the moments of inertia of a rigid member. For an advanced treatment of the inertia representation for rigid multibody systems in terms of natural coordinates, we refer the interested readers to our previous paper [30]. In Appendix A, some fundamental derivations of mass matrices are provided for the sake of completeness.

### 3. Modeling tensegrity structures

Given the formulations of rigid members, the modeling of general Class- $k$  ( $k \geq 1$ ) tensegrity structures additionally requires formulations for tensile cables, torqueless joints, and boundary conditions, which are derived in this section. A system is assumed to have  $n_b$  rigid members and  $n_c$  tensile cables.

#### 3.1. Pin joints and ball joints

A Class- $k$  ( $k > 1$ ) tensegrity system allows the use of frictionless pin joints (or ball joints in the 3D case), each of which can connect up to  $k$  different rigid

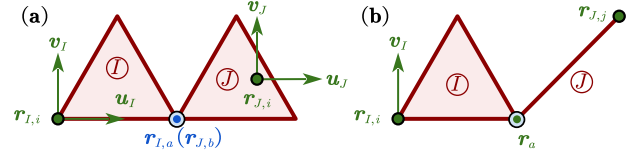


Figure 4: (a) Two 2D rigid bodies or (b) a 2D rigid body and a 2D rigid bar connected by a pin joint, which is represented by a circle filled with light blue.

members. Depending on the placements of basic points, there are two modeling methods.

The first is a general method, as exemplified by Fig. 4(a), where a pin joint pins point  $a$  of rigid body  $\mathcal{I}$  on point  $b$  of rigid body  $\mathcal{J}$ , and consequently imposing a set of extrinsic constraints

$$\Phi^{\text{ex}}(\mathbf{q}_I, \mathbf{q}_J) = \mathbf{r}_{I,a} - \mathbf{r}_{J,b} = \mathbf{C}_{I,a}\mathbf{q}_I - \mathbf{C}_{J,b}\mathbf{q}_J = \mathbf{0}, \quad (19)$$

where (16) is used for the second equality, and the natural coordinates of the two rigid bodies are  $\mathbf{q}_I = [\mathbf{r}_{I,i}^T, \mathbf{u}_I^T, \mathbf{v}_I^T]^T$  and  $\mathbf{q}_J = [\mathbf{r}_{J,i}^T, \mathbf{u}_J^T, \mathbf{v}_J^T]^T$ , respectively.

The second method is to share the basic points between rigid members, as exemplified by Fig. 4(b), where a pin joint is located at the basic point  $a$ . So we have natural coordinates  $\mathbf{q}_I = [\mathbf{r}_{I,i}^T, \mathbf{r}_a^T, \mathbf{v}_I^T]^T$  for the rigid body  $\mathcal{I}$ , and  $\mathbf{q}_J = [\mathbf{r}_a^T, \mathbf{r}_{J,j}^T]^T$  for the rigid bar  $\mathcal{J}$ : they share the vector  $\mathbf{r}_a$ .

If a pin joint connects  $k$  ( $k > 2$ ) rigid members, it can be modeled as  $k-1$  pin joints overlapping at one place.

Ball joints in the 3D case can be modeled in the same way, owing to the unifying form (16).

The second method has computational advantages over the first one because it needs no extrinsic constraint, and it reduces the number of system's coordinates. Owing to the exhaustion in deriving different combinations of the natural coordinates (Sec. 2.1), up to four (or three) basic points of a 3D (or 2D) rigid body can be used for sharing with other rigid members. Therefore, the second method is generally sufficient to model most Class- $k$  ( $k > 1$ ) tensegrities, and the extrinsic constraints (19) are rarely needed.

#### 3.2. Boundary conditions

In practice, most tensegrity systems have some members with prescribed motions, such that their positions, velocities, and accelerations are either partly or entirely given. For example, a rigid member could be pin-jointed to a base, or a cable could have its one endpoint tied to the ground. It would be cumbersome to derive case-by-case formulations for these prescribed rigid members and endpoints. Alternatively, we can extend the above derivations, but also without loss of flexibility, by separating the prescribed and free (unprescribed) coordinates. To do this, let's denote the numbers of prescribed, free, and total coordinates for the rigid member  $\mathcal{I}$  by  $\tilde{n}_I$ ,  $\check{n}_I$ , and  $n_I = \tilde{n}_I + \check{n}_I$ , respectively, and for the system by  $\tilde{n}$ ,  $\check{n}$ , and  $n = \tilde{n} + \check{n}$ , respectively. Then, the separation and reintegration of the coordinates of the rigid member  $\mathcal{I}$  and of the system are defined by

$$\begin{pmatrix} \tilde{\mathbf{q}}_I \\ \check{\mathbf{q}}_I \end{pmatrix} = \begin{bmatrix} \tilde{\mathbf{E}}_I^T \\ \check{\mathbf{E}}_I^T \end{bmatrix} \mathbf{q}_I, \quad \mathbf{q}_I = \begin{bmatrix} \tilde{\mathbf{E}}_I & \check{\mathbf{E}}_I \end{bmatrix} \begin{pmatrix} \tilde{\mathbf{q}}_I \\ \check{\mathbf{q}}_I \end{pmatrix}, \quad \begin{pmatrix} \tilde{\mathbf{q}} \\ \check{\mathbf{q}} \end{pmatrix} = \begin{bmatrix} \tilde{\mathbf{E}}^T \\ \check{\mathbf{E}}^T \end{bmatrix} \mathbf{q}, \quad \text{and} \quad \mathbf{q} = \begin{bmatrix} \tilde{\mathbf{E}} & \check{\mathbf{E}} \end{bmatrix} \begin{pmatrix} \tilde{\mathbf{q}} \\ \check{\mathbf{q}} \end{pmatrix}, \quad (20)$$

where  $\tilde{q}_I \in \mathbb{R}^{\tilde{n}_I}$  and  $\tilde{q} \in \mathbb{R}^{\tilde{n}}$  are prescribed coordinates;  $\check{q}_I \in \mathbb{R}^{\check{n}_I}$  and  $\check{q} \in \mathbb{R}^{\check{n}}$  are free coordinates;  $[\tilde{\mathbf{E}}_I, \check{\mathbf{E}}_I] \in \mathbb{Z}^{\tilde{n}_I \times \tilde{n}_I}$  and  $[\tilde{\mathbf{E}}, \check{\mathbf{E}}] \in \mathbb{Z}^{\tilde{n} \times \tilde{n}}$  are constant orthonormal matrices that only have zeros and ones as elements.

Additionally, let's define a special coordinates vector  $\mathbf{q}_0^T = [\tilde{r}_{0,1}^T, \dots, \tilde{r}_{0,\tilde{n}_p}^T]^T$  concatenating a list of  $\tilde{n}_p$  prescribed points. And, for the sake of consistency, define  $\check{r}_0 = 0$ ,  $n_0 = \tilde{n}_0 = m \times \tilde{n}_p$ , and  $\mathbf{C}_{0,i} = \mathbf{c}_{0,i}^T \otimes \mathbf{I}_m$ , where  $\mathbf{c}_{0,i} \in \mathbb{Z}^{\tilde{n}_p}$  are zeros except that the  $i$ th element equals to 1. Consequently,  $\tilde{\mathbf{E}}_0$  is an identity matrix and  $\check{\mathbf{E}}_0$  is an empty matrix, and the  $i$ th prescribed point can be expressed in the same form of (16) as

$$\mathbf{r}_{0,i} = \tilde{\mathbf{r}}_{0,i} = \mathbf{C}_{0,i} \mathbf{q}_0, \quad \text{for } i = 1, \dots, \tilde{n}_p. \quad (21)$$

The relations between the system's coordinates and those of rigid members and prescribed points are given by

$$\mathbf{q}_I = \mathbf{T}_I \mathbf{q} = \tilde{\mathbf{T}}_I \tilde{\mathbf{q}} + \check{\mathbf{T}}_I \check{\mathbf{q}}, \quad \text{for } I = 0, \dots, n_b, \quad (22)$$

where  $\mathbf{T}_I, \tilde{\mathbf{T}}_I = \mathbf{T}_I \tilde{\mathbf{E}}$ , and  $\check{\mathbf{T}}_I = \mathbf{T}_I \check{\mathbf{E}}$  are constant matrices that select the right elements from the system, and also properly embody the sharing of basic points as presented in Sec. 3.1. Consequently, the relations for velocities and accelerations are simply  $\dot{\mathbf{q}}_I = \mathbf{T}_I \dot{\mathbf{q}}$  and  $\ddot{\mathbf{q}}_I = \mathbf{T}_I \ddot{\mathbf{q}}$ , respectively. On the other hand, the variation should exclude the prescribed coordinates as

$$\delta \mathbf{q}_I = \check{\mathbf{T}}_I \delta \check{\mathbf{q}}. \quad (23)$$

Note that the relations (20) and (22) are actually implemented as index-selecting methods in the computer code so that expensive matrix multiplications are avoided.

Last but not the least, any intrinsic constrains in (5), (10), and (13) and extrinsic constrains in (19) that contain no free coordinates should be dropped. The remaining constraints are collected by  $\check{\Phi}(\mathbf{q})$ , whose Jacobian matrix is defined by  $\check{\mathbf{A}}(\mathbf{q}) = \partial \check{\Phi} / \partial \check{\mathbf{q}}$ .

### 3.3. Generalized forces

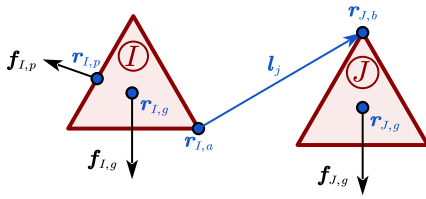


Figure 5: Two 2D rigid bodies subjected to gravity, a concentrated force, and tension forces of a cable. The points of action are colored in blue.

Using (16) and (21) to (23), the position and its variation of a point of action  $p$  on the rigid member  $\textcircled{I}$  are, respectively,

$$\mathbf{r}_{I,p} = \mathbf{C}_{I,p} \mathbf{T}_I \mathbf{q} \quad \text{and} \quad \delta \mathbf{r}_{I,p} = \mathbf{C}_{I,p} \check{\mathbf{T}}_I \delta \check{\mathbf{q}}. \quad (24)$$

Consider a concentrated force  $f_{I,p}$  exerted on point  $p$ , as shown on the left of Fig. 5, the virtual work done by  $f_{I,p}$  is  $\delta W_{I,p} = \delta \mathbf{r}_{I,p}^T f_{I,p} = \delta \check{\mathbf{q}}^T \check{\mathbf{F}}_{I,p}$ , where

$$\check{\mathbf{F}}_{I,p} = \check{\mathbf{T}}_I^T \mathbf{C}_{I,p}^T f_{I,p} \quad (25)$$

is the generalized force for  $f_{I,p}$ .

In particular, the gravity force  $f_{I,g}$  is exerted on the mass center  $\mathbf{r}_{I,g}$ . Therefore, the generalized gravity force for the rigid member  $\textcircled{I}$  is given by  $\check{\mathbf{F}}_{I,g} = \check{\mathbf{T}}_I^T \mathbf{C}_{I,g}^T f_{I,g}$ , which is a constant vector.

Also note that (25) still holds for a prescribed point (21), because in that case,  $\check{\mathbf{T}}_I$  would be a zero matrix.

### 3.4. Tensile cables

In this paper, we adopt a common practice [22, 26, 36] by assuming the cables are massless, so that their inertia forces are ignored and only their tension forces acting on the rigid members need to be formulated.

Suppose the  $j$ th cable connects point  $a$  of the rigid member  $\textcircled{I}$  and point  $b$  of the rigid member  $\textcircled{J}$ , as shown in Fig. 5. It can be represented by a vector

$$\mathbf{l}_j = \mathbf{r}_{J,b} - \mathbf{r}_{I,a} = \mathbf{C}_{J,b} \mathbf{T}_J \mathbf{q} - \mathbf{C}_{I,a} \mathbf{T}_I \mathbf{q} = \mathbf{J}_j \mathbf{q} \quad (26)$$

where we use (24) and  $\mathbf{J}_j = \mathbf{C}_{J,b} \mathbf{T}_J - \mathbf{C}_{I,a} \mathbf{T}_I$  is a constant matrix. Consequently, the current length and its time derivative of the cable are given by, respectively,

$$l_j = \sqrt{\mathbf{l}_j^T \mathbf{l}_j} = \sqrt{\mathbf{q}^T \mathbf{U}_j \mathbf{q}} \quad \text{and} \quad \dot{l}_j = \frac{\dot{\mathbf{l}}_j^T \mathbf{l}_j}{\sqrt{\mathbf{l}_j^T \mathbf{l}_j}} = \frac{(\mathbf{q}^T \mathbf{U}_j \dot{\mathbf{q}})}{l_j}, \quad (27)$$

where  $\mathbf{U}_j = \mathbf{J}_j^T \mathbf{J}_j$  is also constant.

Define the force density by  $\gamma_j = f_j / l_j$ , where  $f_j$  is the tension force magnitude. Then, the tension force is given by either  $\mathbf{f}_j = f_j \hat{\mathbf{l}}_j$  or  $\mathbf{f}_j = \gamma_j \mathbf{l}_j$ , where  $\hat{\mathbf{l}}_j = \mathbf{l}_j / l_j$  is the unit direction vector.

Note that a cable generates a pair of tension forces exerted on points  $a$  and  $b$  with opposite directions. Therefore, according to (25), the generalized tension force for the  $j$ th cable reads

$$\check{\mathbf{Q}}_j = \check{\mathbf{T}}_I^T \mathbf{C}_{I,a}^T f_j - \check{\mathbf{T}}_J^T \mathbf{C}_{J,b}^T f_j = -\check{\mathbf{E}}^T \mathbf{J}_j^T f_j \quad (28)$$

Consequently, the system's generalized tension force is the sum over all cables

$$\check{\mathbf{Q}} = \sum_{j=1}^{n_c} (-\check{\mathbf{E}}^T \mathbf{J}_j^T f_j) = -\check{\mathbf{E}}^T \bigoplus_{j=1}^{n_c} (\mathbf{J}_j^T l_j) \gamma \quad (29)$$

where  $\gamma = [\gamma_1, \dots, \gamma_{n_c}]^T$  collects the force densities and  $\oplus$  means the direct sum of matrices. Expression (29) shows the system's generalized tension force is linear in the cables' force densities. This notable property is also found in the dynamics framework for "bars-only" tensegrities by Skelton et al. [25, 26]. It is beneficial for the design of cable-based control schemes, which, however, will not be elaborated in this paper and subject to further research.

Expression (29) allows any constitutive laws of the cables. In the following, we adopt a common practice by assuming linear stiffness, linear damping, and a slacking behavior. Denote the rest length by  $\mu_j$ , the stiffness coefficient by  $\kappa_j$ , and the damping coefficient by  $\eta_j$ . Then, the tension force magnitude is given by

$$f_j = \begin{cases} f_j^+, & \text{if } f_j^+ \geq 0 \text{ and } l_j \geq \mu_j \\ 0, & \text{else} \end{cases} \quad \text{with } f_j^+ = \kappa_j (l_j - \mu_j) + \eta_j \dot{l}_j. \quad (30)$$

#### 4. Static analysis formulations

Suppose a potential  $V(q)$  is given as a function of the system's total coordinates, then the generalized potential force is given by  $\check{G} = -\partial V(q)/\partial \check{q}^T$ . Because  $\check{\Phi}$  is holonomic, we can define the augmented potential function as  $\Pi = V - \check{\Phi}^T \lambda$ , where  $\lambda$  denotes the Lagrange multipliers. Then, according to the Lagrange-d'Alembert principle, we have the static equation of the system:

$$\begin{cases} -\check{Q} - \check{F}^{\text{ex}} + \frac{\partial \Pi}{\partial \check{q}^T} = -\check{F} - \check{A}^T \lambda = \mathbf{0} \\ -\frac{\partial \Pi}{\partial \lambda^T} = \check{\Phi} = \mathbf{0} \end{cases} \quad (31a)$$

where  $\check{F} = \check{G} + \check{Q} + \check{F}^{\text{ex}}$  includes the generalized potential force  $\check{G}$ , the generalized tension force  $\check{Q}$ , and any other external generalized forces  $\check{F}^{\text{ex}}$ .

We should point out that, as long as the constitutive law of the cables can be transformed into polynomials, the static equation (31) is compatible with our previous work [37] on the *forward* statics problems of tensegrity systems, which are readily solved by the homotopy continuation method, and therefore will not be elaborated here.

For *inverse* statics problems, which solve for the cable variables from a known configuration of the system, it is possible to eliminate the constraint forces first. To do this, define a matrix  $\check{N}$  whose columns are a set of linearly independent basis vectors of the nullspace of  $\check{A}$ , such that  $\check{A}\check{N} = \mathbf{0}$ . Then, left-multiplying (31a) by  $\check{N}^T$  and using (29) lead to

$$\check{N}^T \check{E}^T \bigoplus_{j=1}^{n_c} (J_j^T l_j) \gamma = \check{N}^T (\check{G} + \check{F}^{\text{ex}}), \quad (32)$$

which are a set of linear equations for the force densities  $\gamma$ . After solving (32), the Lagrange multipliers can be recovered from  $\lambda = -(\check{A}\check{A}^T)^{-1} \check{A}\check{F}$ .

When the constitutive law (30) is adopted and the inverse statics (32) is employed to solve for the rest lengths of cables, the following formulations can be used. Let  $\ell = [l_1, \dots, l_{n_c}]^T$  and  $\mu = [\mu_1, \dots, \mu_{n_c}]^T$  collect the lengths and rest lengths, respectively, of all cables. Suppose the cables are in tension, then the force density is given by

$$\gamma_j = f_j/l_j = k_j(l_j - \mu_j)/l_j \quad (33)$$

Substituting (33) into (32) and rearranging the terms, we have a system of linear equations for the rest lengths  $\mu$ :

$$B\mu = b \quad (34)$$

where matrix  $B$  and vector  $b$  are given by, respectively,

$$B = \check{N}^T \check{E}^T \bigoplus_{j=1}^{n_s} (J_j^T k_j \hat{l}_j) \quad \text{and} \quad b = \check{N}^T \check{E}^T \bigoplus_{j=1}^{n_s} (J_j^T k_j \hat{l}_j) \ell - \check{N}^T (\check{G} + \check{F}^{\text{ex}}) \quad (35)$$

#### 5. Dynamic analysis formulations

##### 5.1. Dynamic equation

Recalling the rigid member's kinetic energy (17) and the coordinate selection (22), the system's kinetic energy is simply the sum over all rigid member  $T =$

$\sum_{I=1}^{n_b} T_I = \frac{1}{2} \dot{q}^T M \dot{q}$ , where  $M = \sum_{I=1}^{n_b} T_I^T M_I T_I$  is constant mass matrix. Then, the generalized inertial force is derived with respect to the free coordinates:

$$\frac{d}{dt} \left( \frac{\partial T}{\partial \dot{q}^T} \right) = \frac{d}{dt} (\dot{M} \dot{q}) = \frac{d}{dt} (\dot{M} (\check{E} \dot{q} + \check{E} \dot{\check{q}})) = \check{M} \ddot{q} + \check{M} \ddot{\check{q}} \quad (36)$$

where  $\dot{M} = \check{E}^T \dot{M}$ ,  $\check{M} = \dot{M} \check{E}$ , and  $\check{M} = \dot{M} \check{E}$  are different mass matrices that will be used later.

For the dynamics of a tensegrity system, the Lagrange-d'Alembert principle states that the virtual work vanishes for all inertial forces, generalized forces, and constraint forces acting on the virtual displacement:

$$\delta \check{q}^T (\check{M} \ddot{q} + \check{M} \ddot{\check{q}}) - \delta \check{q}^T \check{F} - \delta \check{q}^T (\check{A}^T \lambda) = 0 \quad (37)$$

Noting that  $\forall \delta \check{q} \in \check{N}$ , (37) leads to the Lagrange's equation of the first kind

$$\check{M} \ddot{q} + \check{M} \ddot{\check{q}} - \check{G}(q) - \check{Q}(q, \dot{q}, \mu) - \check{F}^{\text{ex}}(q, \dot{q}, t) - \check{A}^T(q) \lambda = \mathbf{0} \quad (38a)$$

$$\check{\Phi}(q) = \mathbf{0} \quad (38b)$$

where the dependency is explicated, and the rest lengths  $\mu$  will be used as actuation values. One should also keep in mind that  $q$  contains prescribed coordinates  $\bar{q}$ , which, along with  $\dot{\bar{q}}$  and  $\ddot{\bar{q}}$ , are interpreted as known functions of time  $t$ .

Thanks to the use of natural coordinates, the dynamic equation (38) gets rid of trigonometric functions as well as inertia quadratic velocity terms for centrifugal and Coriolis forces, leaving a constant mass matrix.

For later use, the differential part (38a) can be rewritten as

$$\dot{p} - \check{F} - \check{A}^T \lambda = \mathbf{0} \quad (39)$$

where  $\dot{p} = \partial T / \partial \dot{q}^T = \dot{M} \dot{q}$  is the generalized momentum.

##### 5.2. Linearized dynamics around static equilibrium

For tensegrity structures bearing static loads, such as self-weight, it is useful to derive the linearized dynamics for structural analysis.

Consider a system's state with small perturbations in the free coordinates and Lagrange multipliers as

$$q = q_e + \check{E} \delta \check{q}, \quad \dot{q} = \dot{q}_e + \check{E} \delta \dot{\check{q}}, \quad \ddot{q} = \ddot{q}_e + \check{E} \delta \ddot{\check{q}}, \quad \text{and} \quad \lambda = \lambda_e + \delta \lambda, \quad (40)$$

where  $\dot{q}_e = \ddot{q}_e = \mathbf{0}$ , and  $(q_e, \lambda_e)$  satisfies the static equation (31). Substituting (40) into (38) and expanding it in Taylor series to the first order lead to

$$\left\{ \begin{aligned} \check{M} \delta \ddot{\check{q}} - \frac{\partial \check{F}}{\partial \dot{\check{q}}} \delta \dot{\check{q}} - \frac{\partial \check{F}}{\partial \check{q}} \delta \check{q} - \frac{\partial (\check{A}^T \lambda_e)}{\partial \check{q}} \delta \check{q} - \check{A}^T \delta \lambda = \mathbf{0} \\ \check{A} \delta \check{q} = \mathbf{0} \end{aligned} \right. \quad (41a)$$

$$\quad (41b)$$

Recall that  $\check{N}$  is a basis of the nullspace of  $\check{A}$ . So left-multiplying (41a) by  $\check{N}^T$  eliminates the last term. And (41b) is solved by  $\delta \check{q} = \check{N} \xi$ , where  $\xi$  are independent variables, which is then substituted back to (41a) to yield

$$M \ddot{\xi} + C \dot{\xi} + K \xi = \mathbf{0} \quad (42)$$

where

$$M = \check{N}^T \check{M} \check{N}, \quad C = \check{N}^T \left( \frac{-\partial \check{F}}{\partial \dot{\check{q}}} \right) \check{N}, \quad \text{and} \quad K = \check{N}^T \left( \frac{-\partial \check{F}}{\partial \check{q}} - \frac{\partial (\check{A}^T \lambda_e)}{\partial \check{q}} \right) \check{N} \quad (43)$$

are the reduced-basis mass matrix, reduced-basis tangent damping matrix, and reduced-basis tangent stiffness matrix, respectively. The partial derivatives of  $\tilde{\mathcal{Q}}$ , which are needed to evaluate  $C$  and  $\mathcal{K}$ , are provided in Appendix B.

At this point, we have a standard linear dynamic system (42), which can be used for the modal analysis of general tensegrity structures. For simplicity, consider free vibration with no damping ( $C = \mathbf{0}$ ) and no external forces ( $F^{\text{ex}} = \mathbf{0}$ ), then the solution to (42) boils down to the generalized eigenvalue problem

$$(\mathcal{K} - \omega_{(r)}^2 \mathcal{M}) \xi_{(r)} = \mathbf{0} \quad (44)$$

where  $\omega_{(r)}$  is the natural frequency of the  $r$ th mode;  $\xi_{(r)}$  is the mode shapes in the independent variables, which can be normalized with respect to mass by  $\hat{\xi}_{(r)} = \frac{1}{\sqrt{m_{(r)}}} \xi_{(r)}$ , where  $m_{(r)} = \xi_{(r)}^T \mathcal{M} \xi_{(r)}$ . Then, the mode shapes in the natural coordinates can be obtained through

$$\mathbf{q}_{(r)} = \mathbf{q}_e + \tilde{E} \delta \tilde{\mathbf{q}}_{(r)} = \mathbf{q}_e + \tilde{E} \tilde{N} \hat{\xi}_{(r)} \quad (45)$$

### 5.3. Numerical analysis of nonlinear dynamics

For constrained nonlinear dynamics of tensegrity systems in the form of differential-algebraic equations (DAEs) (38), a numerical integration scheme must not only resolve the differential part (38a) but also satisfy the algebraic part (38b), which includes the intrinsic constraints for rigid members and possible extrinsic constraints for torqueless joints. In this regard, several integrators are available, such as the generalized- $\alpha$  method [38] and the constrained variational integrators. In this paper, the Zu-class symplectic scheme [39, 40] is adopted for two reasons: firstly, it has no artificial dissipation, which is a desirable feature for long-time simulations of space structures, such as tensegrity space booms [41] and space habitats [12]; secondly, it also has computational advantages: it is a one-timestep scheme; it is a position-momentum method, so no need to compute accelerations (and acceleration-like variables as in the generalized- $\alpha$  method); it has no need to compute the partial derivatives of the constraint force. Nonetheless, to make it applicable to the governing DAEs (38), a rework is needed to accommodate non-conservative forces and boundary conditions as follows.

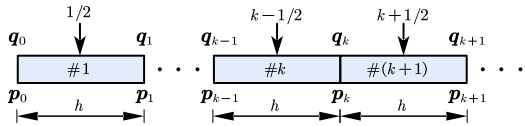


Figure 6: Equally spaced segments of the time domain. Each segment has two endpoints and one midpoint. The state vector  $(\mathbf{q}_k, \mathbf{p}_k)$  is located at endpoint  $k$ .

As illustrated in Fig. 6, the time domain is divided into equally spaced segments, where  $h$  is the timestep and  $(\mathbf{q}_k, \mathbf{p}_k)$  denotes the state vector at the segments' endpoints. At each endpoint, we demand that the differential equation (39) holds as

$$\dot{\mathbf{p}}_k - \tilde{F}_k - \tilde{A}^T(\mathbf{q}_k) \lambda_k = \mathbf{0} \quad (46)$$

Then, substituting central difference approximations

$$\begin{aligned} \dot{\mathbf{p}}_k &\approx \frac{1}{h} (\tilde{\mathbf{p}}_{k+1/2} - \tilde{\mathbf{p}}_k + \tilde{\mathbf{p}}_k - \tilde{\mathbf{p}}_{k-1/2}), \quad \tilde{F}_k \approx \frac{1}{2} (\tilde{F}_{k-1/2} + \tilde{F}_{k+1/2}), \quad \text{and} \\ \lambda_k &\approx \frac{1}{2} (\lambda_{k-1/2} + \lambda_{k+1/2}) \end{aligned} \quad (47)$$

into (46) leads to a discrete scheme

$$\frac{\tilde{\mathbf{p}}_{k+1/2} - \tilde{\mathbf{p}}_k + \tilde{\mathbf{p}}_k - \tilde{\mathbf{p}}_{k-1/2}}{h} - \frac{\tilde{F}_{k-1/2} + \tilde{F}_{k+1/2}}{2} - \tilde{A}(\mathbf{q}_k)^T \frac{\lambda_{k-1/2} + \lambda_{k+1/2}}{2} = \mathbf{0} \quad (48)$$

where the midpoint approximations are

$$\begin{aligned} \mathbf{q}_{k+1/2} &\approx \frac{1}{2} (\mathbf{q}_k + \mathbf{q}_{k+1}), \quad \dot{\mathbf{q}}_{k+1/2} \approx \frac{1}{h} (\mathbf{q}_{k+1} - \mathbf{q}_k), \\ \tilde{\mathbf{p}}_{k+1/2} &\approx \frac{1}{h} \tilde{M}(\mathbf{q}_{k+1} - \mathbf{q}_k), \quad \text{and} \quad \tilde{F}_{k+1/2} \approx \tilde{F}(\mathbf{q}_{k+1/2}, \dot{\mathbf{q}}_{k+1/2}, t_{k+1/2}) \end{aligned} \quad (49)$$

Note that (48) is actually a two-timestep scheme, but can be converted to a one-timestep scheme as follows. As illustrated in Fig. 6, the scheme (48) at endpoint  $k$  have terms in both segments  $\#k$  and  $\#(k+1)$ . Taking the limit  $t_{k-1} \rightarrow t_k$ , we have

$$\lim_{h \rightarrow 0} \frac{\tilde{\mathbf{p}}_k - \tilde{\mathbf{p}}_{k-1/2}}{h/2} = \dot{\mathbf{p}}_k, \quad \lim_{h \rightarrow 0} \tilde{F}_{k-1/2} = \tilde{F}_k, \quad \text{and} \quad \lim_{h \rightarrow 0} \lambda_{k-1/2} = \lambda_k \quad (50)$$

which shows that the terms in segment  $\#k$  tend to (46), so they can be dropped, leaving

$$\tilde{\mathbf{p}}_{k+1/2} - \tilde{\mathbf{p}}_k - \frac{h}{2} \tilde{F}_{k+1/2} - \frac{h}{2} \tilde{A}(\mathbf{q}_k)^T \lambda_{k+1/2} = \mathbf{0} \quad (51)$$

Similarly, taking the limit  $t_{k+1} \rightarrow t_k$  in (48) leads to

$$\tilde{\mathbf{p}}_k - \tilde{\mathbf{p}}_{k-1/2} - \frac{h}{2} \tilde{F}_{k-1/2} - \frac{h}{2} \tilde{A}(\mathbf{q}_k)^T \lambda_{k-1/2} = \mathbf{0} \quad (52)$$

Then, applying (52) to endpoint  $k+1$ , and combining it with (51) as well as the constraint equations, lead to a new scheme:

$$\begin{cases} \frac{1}{h} \tilde{M}(\mathbf{q}_{k+1} - \mathbf{q}_k) - \tilde{\mathbf{p}}_k - \frac{h}{2} \tilde{F}_{k+1/2} - \frac{h}{2} \tilde{A}(\mathbf{q}_k)^T \lambda_{k+1/2} = \mathbf{0} & (53a) \\ \tilde{\mathbf{p}}_{k+1} - \frac{1}{h} \tilde{M}(\mathbf{q}_{k+1} - \mathbf{q}_k) - \frac{h}{2} \tilde{F}_{k+1/2} - \frac{h}{2} \tilde{A}(\mathbf{q}_{k+1})^T \lambda_{k+1/2} = \mathbf{0} & (53b) \\ \tilde{\Phi}(\mathbf{q}_{k+1}) = \mathbf{0} & (53c) \end{cases}$$

In this new scheme, (53a) and (53c) are rearranged as a residual expression

$$\mathbf{Res}(\mathbf{x}_{k+1}) = \begin{pmatrix} -h\tilde{\mathbf{p}}_k + \tilde{M}(\mathbf{q}_{k+1} - \mathbf{q}_k) - \frac{h^2}{2} \tilde{F}_{k+1/2} - s_1 \frac{h^2}{2} \tilde{A}^T(\mathbf{q}_k) \lambda_{k+1/2} \\ \tilde{\Phi}(\mathbf{q}_{k+1}) \end{pmatrix} \quad (54)$$

where  $\mathbf{x}_{k+1} = [\tilde{\mathbf{q}}_{k+1}^T, \lambda_{k+1/2}^T]^T$ , and  $s_1 = 2h^{-2}$  is a scaling factor [42] that is needed for better conditioning of the Jacobian matrix

$$\mathbf{Jac}(\mathbf{x}_{k+1}) = \frac{\partial \mathbf{Res}}{\partial \mathbf{x}_{k+1}} = \begin{bmatrix} \tilde{M} - \frac{h^2}{2} \frac{\partial \tilde{F}_{k+1/2}}{\partial \tilde{\mathbf{q}}_{k+1}} & -\tilde{A}^T(\mathbf{q}_k) \\ \tilde{A}(\mathbf{q}_{k+1}) & \mathbf{0} \end{bmatrix} \quad (55)$$

The residual (54) and its Jacobian (55) allow us to solve for  $\mathbf{x}_{k+1}$  using the Newton-Raphson iteration method. After that,  $\mathbf{x}_{k+1}$  is substituted into (53b) to compute  $\tilde{\mathbf{p}}_{k+1}$  explicitly.

We can observe that the boundary conditions given in terms of  $\tilde{\mathbf{q}}$  is automatically included in  $\mathbf{q}_k$  and  $\mathbf{q}_{k+1}$ , and there is no need to evaluate  $\tilde{\mathbf{q}}$ . Partial derivatives of the constraint force  $\tilde{A}^T(\mathbf{q}) \lambda$ , which are needed for other schemes [38], do not appear in (55).

The partial derivatives of  $\tilde{\mathcal{Q}}$ , which are needed to evaluate the term  $\frac{\partial \tilde{F}_{k+1/2}}{\partial \tilde{\mathbf{q}}_{k+1}}$  in (55), are provided in Appendix B. The complete integration procedure is summarized in Alg. 1.

---

**Algorithm 1:** Modified symplectic integration scheme
 

---

```

input : initial values  $q_0$  and  $\dot{q}_0$ ; timestep  $h$ , total steps  $N$ ;
          maximum iteration  $s_{\max}$ , tolerance  $\epsilon_{\text{tol}}$ 
 $p_0 \leftarrow M\dot{q}_0$ ;
for  $k \leftarrow 0$  to  $N - 1$  do
   $\check{q}_{k+1} \leftarrow \check{q}_k$ ;
   $\lambda_{k+1/2} \leftarrow \mathbf{0}$ ;
   $x_{k+1} \leftarrow [\check{q}_{k+1}^T, \lambda_{k+1/2}^T]^T$ ;
  for  $s \leftarrow 1$  to  $s_{\max}$  do /* Newton-Raphson iteration */
    compute Res by (54);
    if  $\|\mathbf{Res}\| > \epsilon_{\text{tol}}$  then
      compute Jac by (55);
       $\Delta x \leftarrow -(\mathbf{Jac})^{-1} \mathbf{Res}$ ;
       $x_{k+1} \leftarrow x_{k+1} + \Delta x$ ;
    else
      break;
    end
  end
  compute  $\check{p}_k$  by (53b);
   $\dot{\check{q}}_k \leftarrow \check{M}^{-1} (\check{p}_k - \check{M}\dot{\check{q}}_k)$ ;
end

```

---

## 6. Numerical examples

Numerical studies of several dynamic examples are presented in this section. Its aim is three-fold: (1) To verify the proposed modeling framework of tensegrity systems and the integration scheme, by comparing against reference results in terms of trajectories, natural frequencies, and mode shapes; (2) To show the proposed approach's ability to perform nonlinear dynamic analyses with complex conditions, including conservative and non-conservative tension forces, cable-based deployments, gravity loads, and moving boundaries. (3) To show the proposed approach's ability to study the dynamics of tensegrity systems that include both arbitrary rigid bodies and rigid bars. In particular, we present a 2D Class-3 tensegrity tower and a 3D Class-2 deployable tensegrity structure, which exemplify new ways to compose tensegrity structures.

### 6.1. Example 1: Dynamics of a double pendulum

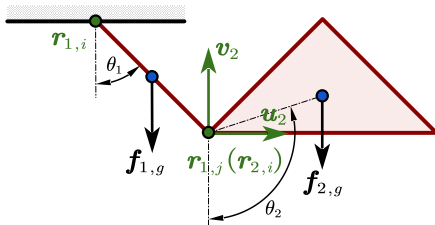


Figure 7: Schematic diagram of a double pendulum in the presence of gravity.

This example is a planar double pendulum, composed of a rigid bar and an isosceles right triangular rigid plate, and subjected only to gravity. It is different from the conventional two-bar double pendulum, and, as such, serves to test

Table 2: Physical parameters of rigid members in example 1.

	Parameter	Value
Bar	Mass	0.026 93 kg
	Moment of Inertia	$1.122 \times 10^{-5}$ kg m <sup>2</sup>
	Length	0.070 71 m
Isosceles right triangle	Mass	0.1271 kg
	Moment of Inertia	$7.063 \times 10^{-5}$ kg m <sup>2</sup>
	Height	0.050 00 m

some fundamental ingredients of the proposed natural coordinates framework for tensegrity system dynamics. The initial configuration and the arrangement of basic points and base vector are shown in Fig. 7. Physical parameters of the two rigid members are listed in Tab. 2.

More importantly, this example is chosen to check if the proposed non-minimal formulations with the integration scheme Alg. 1 can produce accurate results, both in short-time and long-time simulations. In particular, it is compared with the minimal formulation, which uses the two angles  $\theta_1$  and  $\theta_2$  as generalized coordinates leading to a set of ordinary differential equations (ODEs), and then simulated by a 5th order Runge-Kutta method with a maximum timestep  $h_{\max} = 1 \times 10^{-5}$  s. Fig. 8 plots the time histories of the angles and angular velocities for 4-second simulations. It shows the proposed integration scheme, even when using a much larger timestep  $h = 1 \times 10^{-3}$  s, produces results that are in good agreement with the reference solutions, and accurately captures the nonlinear dynamic behaviors of the double pendulum, especially the abrupt changes of angular velocities. Therefore, the timestep for the proposed integration scheme is set to  $h = 1 \times 10^{-3}$  s in all following simulations.

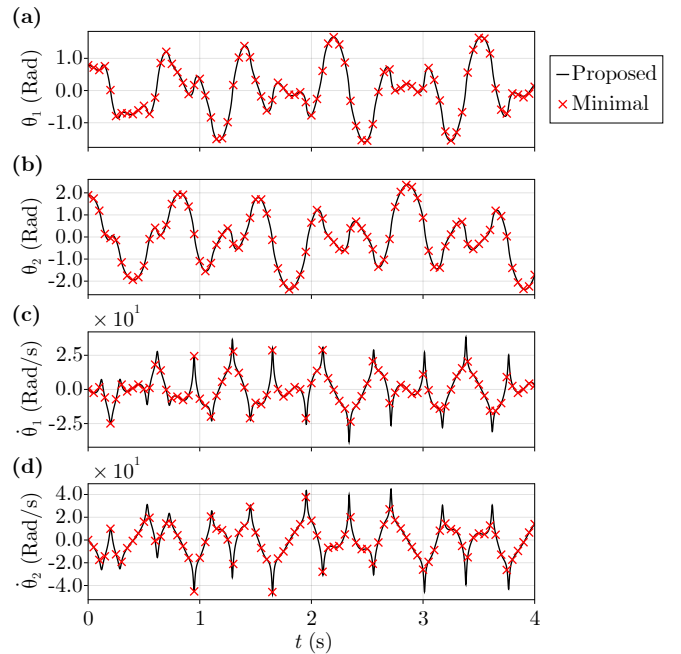


Figure 8: Time histories of angles (a)  $\theta_1$ , (b)  $\theta_2$  and angular velocities  $\dot{\theta}_1$  and  $\dot{\theta}_2$  of the double pendulum.

For long-time simulations, the proposed integration scheme is compared against the generalized- $\alpha$  scheme, in terms of the mechanical energy  $E = T + V$ , which should be conserved. As shown in Fig. 9, for 500-second simulations the system's energy  $E$  is mostly conserved by the proposed method, but gradually damped out by the generalized- $\alpha$  scheme, which uses a typical spectral radius  $\rho_\infty = 0.7$ . This result is reasonable because the spectral radius  $\rho_\infty$  controls the numerical dissipation, which is important to ensure a stable solution for the generalized- $\alpha$  scheme, while the proposed modified symplectic integration scheme has no numerical dissipation.

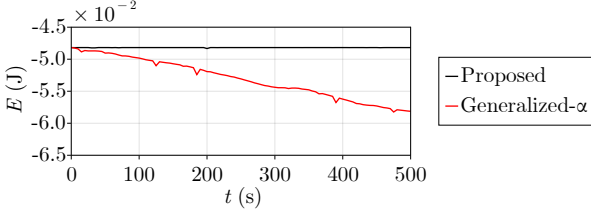


Figure 9: Time history of the mechanical energy  $E$  of the double pendulum.

## 6.2. Example 2: A 2D Class-3 tensegrity tower

This example is a new design of 2D tensegrity structure: 4 rigid bars, 3 isosceles right triangular rigid plates, and 12 cables compose a 3-level tower, as shown in Fig. 10. The vertices of triangles are pin jointed with up to two bars: the apex of triangle ⑤ connects both bars ④ and ⑥, while other vertices connect at most one bar. Thus, it is a Class-3 tensegrity structure by definition.

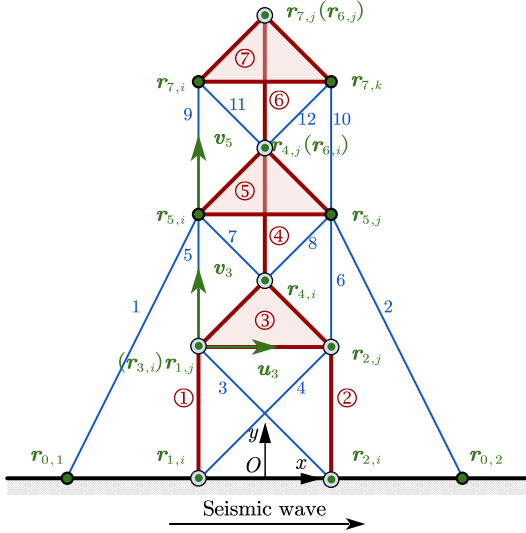


Figure 10: Schematic drawing of the 2D Class-3 tensegrity tower.

Due to the presence of pin joints, the structure's DoFs are reduced to 5. It is pre-stressed redundantly by 12 cables, which have the same stiffness coefficient  $\kappa$  and damping coefficient  $\eta$ . Additionally, the cables 3 to 12, which are essential to the integrity of the structure, have rest lengths being  $\alpha$  times their initial lengths. Cables 1 and 2, which provide auxiliary tensions, have rest lengths being  $\beta$  times their initial lengths. Tab. 3 lists the physical parameters of rigid members and cables for this example. Such a bilateral symmetric setup of

Table 3: Physical parameters of rigid members and cables in example 2.

Parameter	Value	
Mass	0.026 93 kg	
Bars	Moment of Inertia	$2.245 \times 10^{-5} \text{ kg m}^2$
	Length	0.1000 m
	Isosceles right triangles	Same as Example 1
Cables	Stiffness coefficient $\kappa$	$100 \text{ N m}^{-1}$
	Damping coefficient $\eta$	$0 \text{ N s m}^{-1}$ or $0.1000 \text{ N s m}^{-1}$
	Rest length	$\alpha \times \text{Initial length}$ for $j = 1, 2$ $\beta \times \text{Initial length}$ for $j = 3, \dots, 12$

geometry and distribution of tension forces ensures an initial static equilibrium of the structure.

Figure 10 also illustrates how to model this structure by arranging the basic points and base vectors to form natural coordinates: three triangles ③, ⑤, and ⑦ use the three types of natural coordinates RUV, RRV, and RRR, respectively; pin joints are modeled either by the sharing of basic points, such as  $r_{1,j}$  and  $r_{3,i}$ , or by extrinsic constraints, such as that at  $r_{2,j}$ ; the basic points on the ground  $r_{0,1}$ ,  $r_{2,i}$ ,  $r_{0,1}$ , and  $r_{0,2}$  make up the prescribed coordinates.

Therefore, this example covers all the ingredients that are needed to comprehensively test the proposed approach for the dynamics of general 2D tensegrity systems. In the rest of this section, the proposed approach is used to conduct modal analyses and nonlinear dynamic analyses to investigate the effects of cables' properties on the structure's dynamics. The results are also compared with the commercial software Adams for verification.

### 6.2.1. Modal analysis

Since the structure is initially in static equilibrium, its dynamics can be linearized, following the procedure in Sec. 5.2.

For stiffness coefficient  $\kappa = 100 \text{ N m}^{-1}$  and rest length ratios  $\alpha = \beta = 0.9$ , Figs. 11 to 13 show that the natural frequencies and mode shapes produced by the proposed approach are in good agreement with Adams. The maximum relative error of natural frequencies is  $4 \times 10^{-9}$ . And the mode shapes are also reliably computed by the transformation from independent variables to natural coordinates.

Shortening cables' rest lengths can increase the pre-stress level of tensegrity structures, and is shown to be one of the effective ways to change, but not always increase, the natural frequencies. For example, when the pre-stress level increases through reducing rest lengths, [43] shows natural frequencies of tensegrity structures generally increase, but [44] shows that the lowest natural frequency decreases due to the buckling of bars. Here, we also investigate the effects of pre-stress levels on the structure's stiffness. Setting the rest length ratios  $\alpha$  and  $\beta$  from 0.845 to 0.999, the computed natural frequencies are shown in Fig. 14. An interesting phenomenon is observed: when the pre-stress level increases through shortening the cables, the highest two natural frequencies

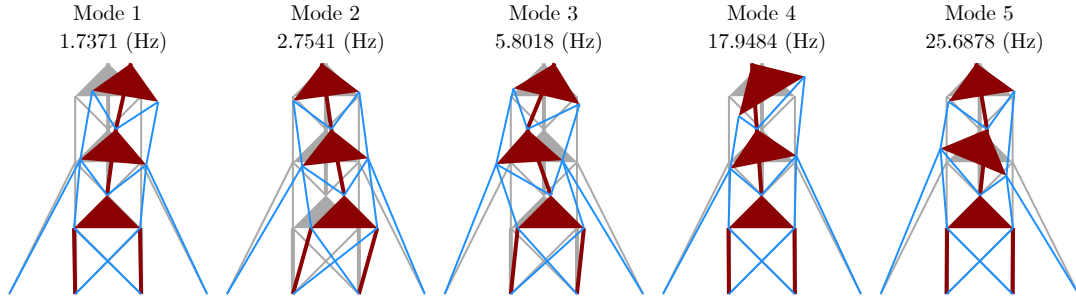


Figure 11: All five mode shapes of the 2D tensegrity tower obtained by the proposed approach.

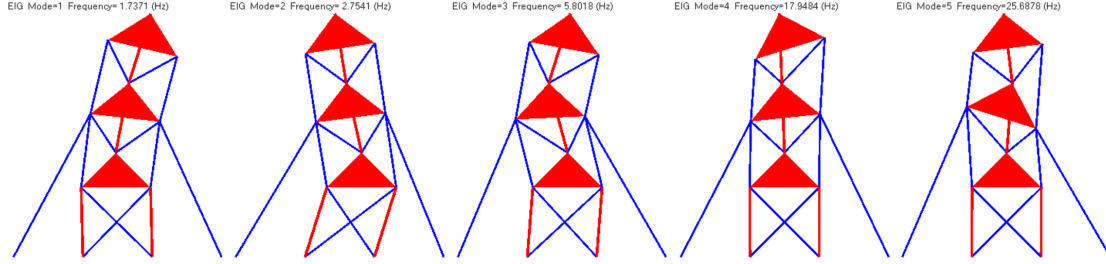


Figure 12: All five mode shapes of the 2D tensegrity tower obtained by Adams.

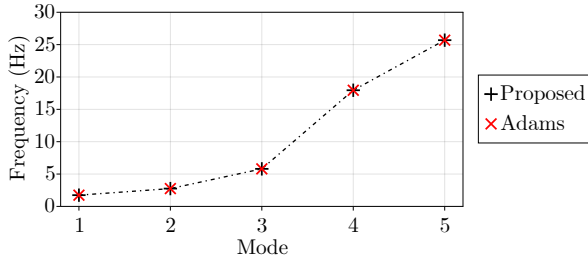


Figure 13: Natural frequencies of the 2D tensegrity tower with respect to the order of vibration mode by the proposed approach and Adams.

increase, but the lowest three ones decrease. In particular, the lowest natural frequency reaches zero at  $\alpha = \beta = 0.845$ , meaning a loss of structural stability. This result is verified by Adams, which are shown as marker points in Fig. 14. This phenomenon bears a notable relationship to the planar Class-2 tensegrity mechanism in [45], where the researchers also found the structural stability is lost when reducing cables' rest lengths. However, further analysis of this instability behavior is beyond the scope of this paper.

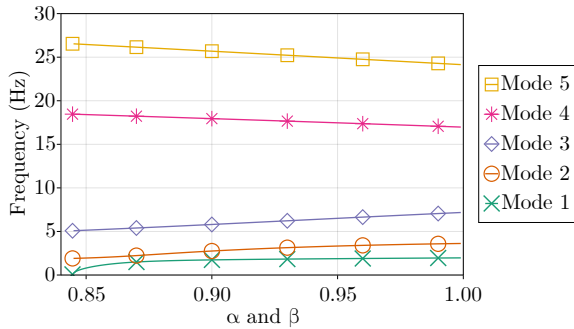


Figure 14: Natural frequencies of the 2D tensegrity tower with respect to rest length ratios  $\alpha$  and  $\beta$ .

### 6.2.2. Numerical analysis of nonlinear dynamics

The next question is whether the structure can sustain simultaneous excitation and loading forces, given the different properties of cables.

Firstly, gravity is loaded along the negative y-axis.

Secondly, a sine seismic wave  $x = 0.01 \sin(6\pi t)$  m is exerted on the ground as a moving boundary condition, through the prescribed points  $r_{0,1}$ ,  $r_{0,2}$ ,  $r_{1,i}$ ,  $r_{2,i}$ .

Thirdly, the rest length ratios are set to  $\alpha = 0.95$  and  $\beta = 0.998$ , which ensure a stable initial state and also give rise to rich dynamics in seismic simulations. Furthermore, four cable setups, with three constitutive laws derived from (30), are considered:

- (1) (UN) Undamped and No slacking:  $f_j = \kappa(l_j - \mu_j)$  with  $\kappa = 100 \text{ N m}^{-1}$ ;
- (2) (DN) Damped and No slacking:  $f_j = \kappa(l_j - \mu_j) + \eta \dot{l}_j$  with  $\kappa = 100 \text{ N m}^{-1}$  and  $\eta = 0.1 \text{ N s m}^{-1}$ ;
- (3) (US) Undamped and Slacking: if  $l_j - \mu_j > 0$ , then  $f_j = \kappa(l_j - \mu_j)$  with  $\kappa = 100 \text{ N m}^{-1}$ , else  $f_j = 0$ .
- (4) (US-AUX) Same as the US setup, except that the seismic wave is exerted only on the bar's endpoints  $r_{1,i}$  and  $r_{2,i}$ , while the auxiliary cables's anchor points  $r_{0,1}$  and  $r_{0,2}$  remain fixed.

The first two setups UD and DN are used to make direct comparisons with Adams, which has no built-in support for slack cables. In the US and US-AUX setups, slack cables are approximated by spline interpolations in Adams, but are implemented exactly in the proposed approach. The US-AUX setup is used to investigate the effects of the auxiliary cables.

Then, nonlinear dynamic simulations are carried out using the proposed integration scheme Alg. 1 for 2 s or until the structure collapses. The time histories of the  $x$ -coordinate of the centroid of triangle ③ is plotted in Fig. 15. It shows a good agreement with Adams, especially for the UN and DN setups.

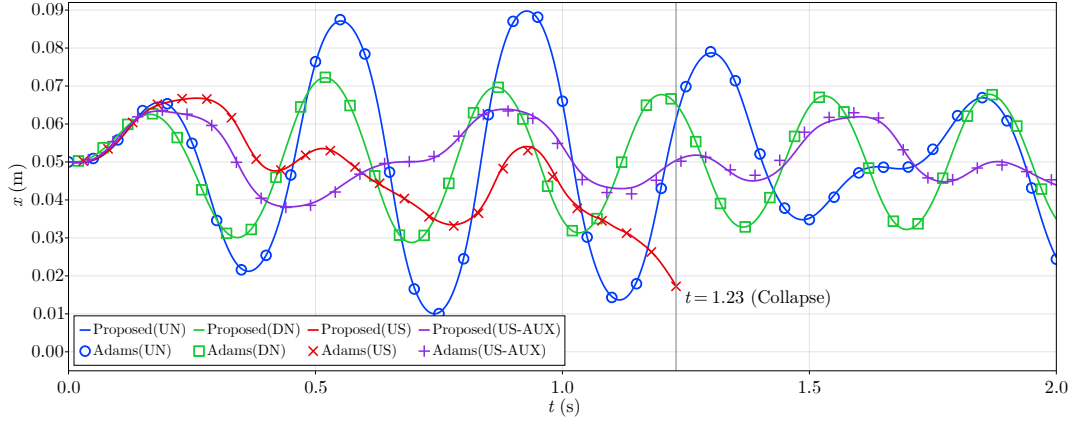


Figure 15: Time histories of the  $x$ -coordinate of the centroid of triangle ③ for the UN, DN, US, and US-AUX setups.

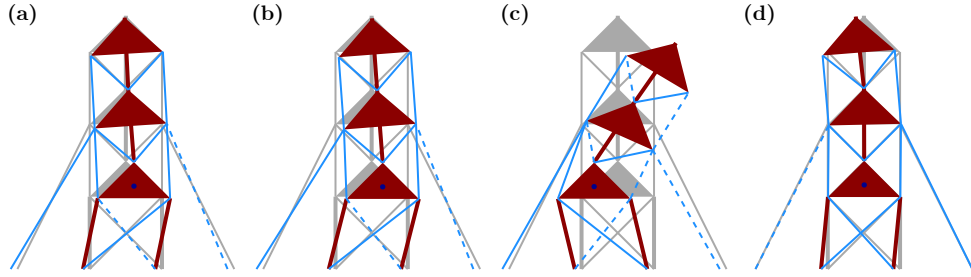


Figure 16: Snapshots of the 2D tensegrity tower at time  $t = 1.23$  s for the (a) UN, (b) DN, (c) US, and (d) US-AUX setups. Blue dashed lines represent (a,b) compressed or (c,d) slack cables.

The discrepancies for the US and US-AUX setups are relatively larger, due to the spline approximation used in Adams.

Figure 16 visualizes the structures in the four setups at  $t = 1.23$  s, which is the time when the structure in the US setup is collapsing: beyond this time the structure will never swing back and will eventually touch the ground. The cables with their current lengths shorter than rest lengths are drawn by blue dash lines. In the UN and DN setups, these are actually springs in compression, while in the US and US-AUX setups these are the slack cables.

Figure 17 compares the occurrences of cables' slacking in the US and US-AUX setups. It shows that almost all cables in the US setup and only four ones in the US-AUX setups went through slacking. And at the time  $t = 1.23$  s, six cables, including five essential ones, are in sustained slacking in the US setup, but only one auxiliary cable is so in the US-AUX setup. These results suggest that the auxiliary cables can provide stabilizing support if their anchor points are fixed.

### 6.3. Example 3: A 3D deployable tensegrity structure

This example is a 3D multi-stage deployable tensegrity structure, which is also a new design in the tensegrity literature to the best of our knowledge. It can be decomposed into three kinds of tensegrity modules:

- (1) A Class-1 tensegrity module composed of two rigid tetrahedrons and six cables, including three outer cables and three inner ones, as shown in Fig. 18(a). Since the two tetrahedrons are not jointed but instead maintain a proper separation through cables' tension forces, it is a Class-1

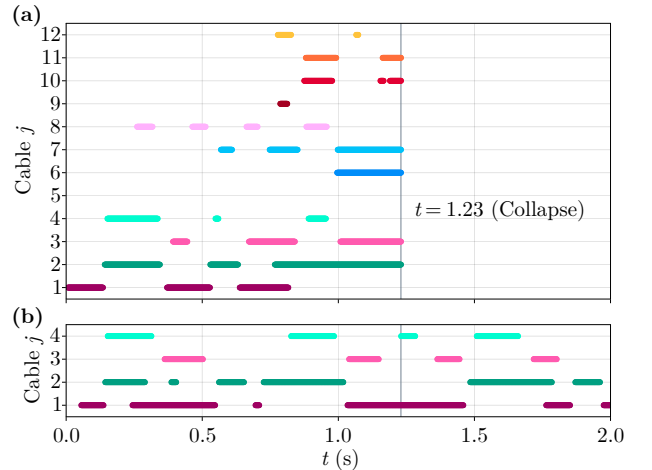


Figure 17: Occurrences of cables' slacking in the (a) US and (b) US-AUX setups. It is also known as a 2-segment Tetraspine [46] in the robotics literature because it resembles the vertebrate spines;

- (2) A Class-2 tensegrity module composed of two jointed rigid tetrahedrons and three cables, as shown in Fig. 18(b). This module bears similarity to the dual-triangle planar tensegrity mechanism [45]. But instead of being limited to planar motions, it can realize spatial rotations around the joint, either passively or actively;
- (3) A 2-stage tensegrity prism module, also known as tensegrity triplex, composed of six bars and twelve cables, as shown in Fig. 18(c). Tensegrity prism is one of the earliest kinds of "bars-only" tensegrity structures [3] with a notable feature of deployability through cable-based actuations

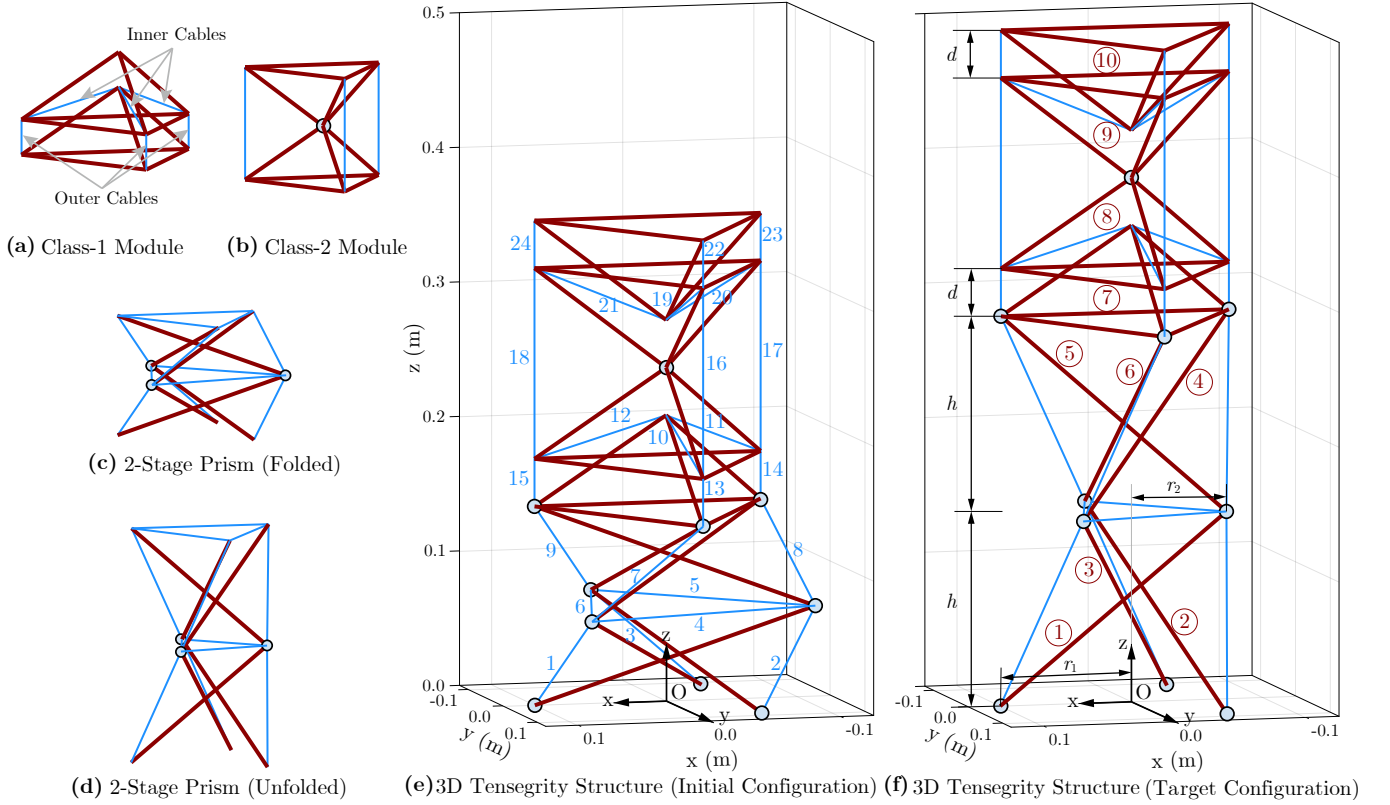


Figure 18: Schematic drawings of (a) a Class-1 tensegrity module, (b) a Class-2 tensegrity module, (c) a folded and (d) an unfolded 2-stage prism, and the (e) initial and (f) target configurations of the 3D deployable tensegrity structure.

[43, 47]. For simplicity, here we assume that each cable can be actuated independently. Fig. 18(d) shows how the 2-stage prism is unfolded after deployment.

These modules compose the whole structure using the tetrahedrons as interfaces. First, the uppermost three cables of the 2-stage prism are replaced by a tetrahedron. Then, a Class-1 module, a Class-2 module, and another Class-1 module are stacked upon the prism one by one. The physical parameters of rigid members and cables for this example are listed in Tab. 4.

This new structure is one of the few examples in the literature that integrate both 3D rigid bodies and 3D rigid bars into one tensegrity system. In this way, it also integrates the functionalities of different modules: in the lower part, the 2-stage prism provides deployability; in the upper part, the Class-2 module provides the function of orientation-tuning, while the Class-1 modules can be used for vibration isolation. In this paper, we focus on its deployability feature, leaving the investigation of other applications to in-depth studies in the future. The structure's configurations before and after deployment are referred to as the initial and target configurations, as shown in Fig. 18(e) and (f), respectively.

Note that this new structure can not be faithfully modeled in Adams, due to the presence of 5-DoF rigid bars. To test the proposed modeling approach and the numerical integration scheme, we consider the problem of deployment simulations in a dynamic environment.

Modeling of the structure is straightforward using the natural coordinates approach. Working from top to bottom, the rigid tetrahedrons can be modeled

by whatever types of natural coordinates for 3D rigid bodies, but for the purpose of verification, the four types of natural coordinates RUVW, RRVW, RRRW, and RRRR are used for the four tetrahedrons ⑩, ⑨, ⑧, and ⑦, respectively; For the 2-stage prism, endpoints of the rigid bars are used as basic points, and those which are jointed to the ground become the prescribed coordinates; Lastly, all ball joints are automatically modeled by the sharing of basic points.

Degrees of freedom can be worked out algebraically as follows. Originally, four rigid tetrahedrons have  $4 \times 6 = 24$  DoFs, while six bars have  $6 \times 5 = 30$  DoFs. Ten ball joints, including one between ⑨ and ⑧, six for the ends of bars ④ to ⑥, and three between bars ① to ③ and the ground, impose  $10 \times 3 = 30$  constraints. Therefore, the system has  $24 + 30 - 30 = 24$  DoFs.

To implement the cable-based actuation for deployment simulations, the rest lengths of the first nine cables  $\mu_1(t)$  to  $\mu_9(t)$  are specified as functions of time  $t$ . On the other hand, the dynamic environment is exemplified by a sine seismic wave  $x(t) = 0.01 \sin(\nu 2\pi t)$  on the ground with a seismic frequency  $\nu$ .

Many studies on deployable tensegrity structures generally regard the deployment as a quasi-static process [9, 48] or a sequence of static equilibria [5], and assume that the dynamic effects can be neglected if the deployment time is sufficiently large. This assumption is obviously not warranted for deployments in dynamic environments, where various factors, such as a moving base, wind loadings, or impact events, could have long-term and/or short-term effects and hinder the success of deployments.

However, this quasi-static view can predict certain dynamic behaviors during

Table 4: Physical parameters of rigid members and cables in example 3.

	Parameter	Value
Bars	Mass	0.080 00 kg
	Moment of Inertia	0.000 322 7 kg m <sup>2</sup>
	Length	0.2200 m
Tetrahedrons	Mass	0.2999 kg
	Center of mass	at height 0.014 82 m above the base triangle
	Principal moments of Inertia	7.664 × 10 <sup>-4</sup> kg m <sup>2</sup> , 7.664 × 10 <sup>-4</sup> kg m <sup>2</sup> and 1.246 × 10 <sup>-3</sup> kg m <sup>2</sup>
	Circumradius of base regular triangle	0.010 00 m
	Height	0.070 71 m
Cables	Stiffness coefficient	1000 N m <sup>-1</sup> for the 2-stage prism 500 N m <sup>-1</sup> for others
	Damping coefficient	2 N s m <sup>-1</sup>
	Rest length	See text and Tab. 5

deployment. In a quasi-static process, the structure's static equilibrium varies continuously, so the natural frequencies would also vary continuously from the initial state to the target state. If the seismic frequency  $\nu$  sits between the natural frequencies of an initial state and a target state, there must be an intermediate state which resonates with this specific seismic frequency during deployment, and consequently leads to severe vibrations or even collapse.

In what follows, we will verify this prediction and thereby test our proposed approach for the dynamic analysis of tensegrity structures in complex conditions. First, the statics and dynamics of the structure in the initial and target states are examined in Secs. 6.3.1 and 6.3.2. Then, deployment simulations are conducted in Sec. 6.3.3.

### 6.3.1. Inverse statics and modal analysis

Both initial and target configurations are straightly upright, as shown in Fig. 18(e) and (f). Therefore, they are uniquely defined by the distances between tetrahedrons  $d$ , the height of a prism stage  $h$ , and the circumradiuses  $r_1$  and  $r_2$ , which are listed in Tab. 5.

Since the system has 24 DoFs and 24 cables, the matrix  $\mathbf{B}$  in (34) is of dimension 24×24. But for both initial and target configurations, the rank of matrix  $\mathbf{B}$  is 21, which means the equations (34) have a 3-dimensional solution set. This is because the Class-1 and Class-2 modules have non-unique solutions for the rest lengths. The Class-2 module can achieve static equilibrium as long as all three cables have the same rest lengths. In the Class-1 module, tension forces of outer cables are determined from the vertical loading as well as the rest lengths of inner cables. Therefore, in order to have a unique solution for the rest lengths, we first specify  $\mu_{16} = \mu_{17} = \mu_{18} = 0.1$  m and  $\mu_{13} = \mu_{14} = \mu_{15} = \mu_{19} =$

$\mu_{20} = \mu_{21} = 0.03$  m. Then, substituting these values into (34) allows solving for other rest lengths. The results are listed in Tab. 5, which together with Tab. 4 completely defines the initial and target static states. As expected, only the first nine cables' rest lengths need to be varied for the deployment. We also verify that there is no slack cable in either state.

Modal analyses are then conducted for both initial and target states to compute the natural frequencies. Note that, different from example 2, gravity is taken into account here for the static equilibrium and consequently in the model analyses, so as to be closer to real-world situations. Fig. 19 shows the first five natural frequencies, excluding duplicates, for both states. Of particular interest is the decrease of the lowest natural frequency from 0.7184 Hz to 0.3270 Hz. This can be attributed to the combined effects of the structure's elevated mass center, the decrease of circumradius  $r_2$ , and the loosening of some cables.

Table 5: Physical parameters of initial and target configurations in example 3.

	Label	Initial	Target
Distance	$d$	0.035 36 m	0.035 36 m
Height	$h$	0.070 71 m	0.1414 m
Circumradius	$r_1$	0.1000 m	0.1000 m
	$r_2$	0.1100 m	0.070 00 m
Cables' rest lengths	(1, 2, 3)	0.1039 m	0.1545 m
	(4, 5, 6)	0.1677 m	0.1109 m
	(7, 8, 9)	0.1045 m	0.1550 m
	(10, 11, 12)	0.072 35 m	0.072 35 m
	(13, 14, 15)	0.030 00 m	0.030 00 m
	(16, 17, 18)	0.1000 m	0.1000 m
	(19, 20, 21)	0.030 00 m	0.030 00 m
	(22, 23, 24)	0.084 12 m	0.084 12 m

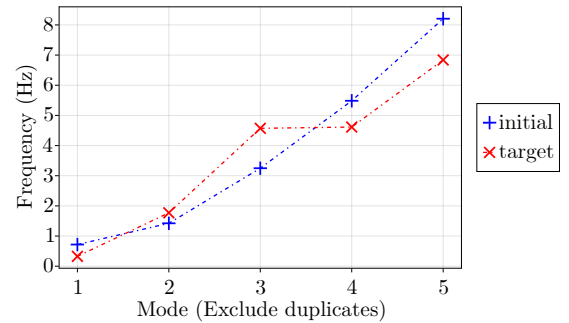


Figure 19: First five natural frequencies, excluding duplicates, of the 3D tensegrity structure in the initial and target states.

### 6.3.2. Seismic simulations

Next, we conduct seismic simulations for both initial and target configurations, starting from their static equilibrium states. The seismic frequency is set

to  $\nu = 0.5$  Hz, which sits approximately in the middle of the two states' lowest natural frequencies.

Fig. 20 plots the trajectories in the  $x$  and  $z$  coordinates of mass centers of the tetrahedrons ⑦ to ⑩ for 15-second seismic simulations. The  $y$  coordinates' changes are smaller than the  $x$  coordinates by one order of magnitude, thus not shown. None of the amplitudes of responses in any coordinates increase with time. These results show that, as expected, the structure starting from both initial and target states undergoes forced vibrations but no resonance with the seismic wave.

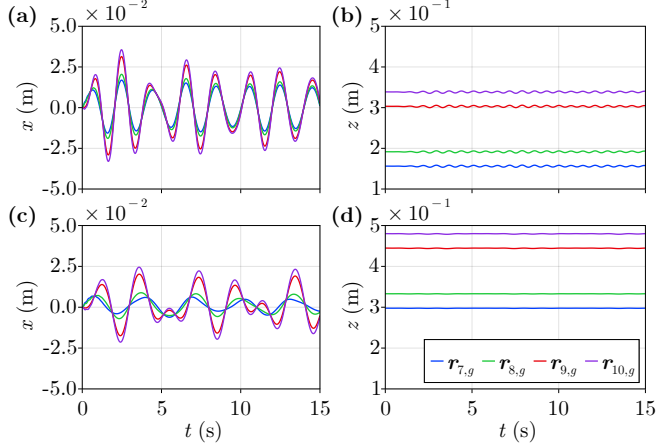


Figure 20: Time histories of the (a,c)  $x$  and (b,d)  $z$  coordinates of  $r_{7,g}$ ,  $r_{8,g}$ ,  $r_{9,g}$ , and  $r_{10,g}$  for the 3D tensegrity structure starting from the (a,b) initial and (c,d) target states.

### 6.3.3. Deployment simulations

In order to conduct deployment simulations, the actuation strategy of the cables' rest lengths must be specified. Specifically, the rest length of the  $j$ th cable is implemented as a function of time

$$\mu_j(t) = (1 - \tau(t))\mu_{j,0} + \tau(t)\mu_{j,1}$$

where the coefficient  $\tau$  takes values from 0 to 1; the initial and target values  $\mu_{j,0}$  and  $\mu_{j,1}$  are taken from Tab. 5. For simplicity, a linear actuation strategy is used: before the deployment duration  $T_d$ , the coefficient  $\tau$  varies linearly, after that,  $\tau$  remains unchanged, as shown in Fig. 21.

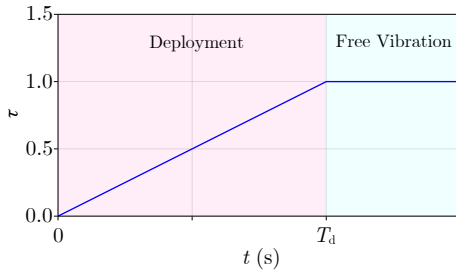


Figure 21: Actuation coefficient  $\tau(t)$  as a function of time  $t$ .

Deployment simulations are then carried out on seismic grounds with different deployment durations  $T_d = 5$  s, 10 s, 15 s and 20 s and different seismic frequencies  $\nu = 0.2$  Hz, 0.5 Hz and 1.0 Hz. Note that the frequencies  $\nu = 0.2$  Hz

and 1.0 Hz are outside of the expected resonance range [0.7184, 0.3270] Hz and also avoid other natural frequency ranges. Deployment simulations on static ground are also conducted to provide reference solutions.

For  $T_d = 10$  s and  $\nu = 0.5$  Hz, snapshots of the structure at times  $t = 1$  s, 5.5 s and 10 s are visualized in Fig. 22. For all deployment simulation cases, trajectories in the  $x$  and  $z$  coordinates of the mass center of tetrahedron ⑩ are plotted in Fig. 23.

These results show that, for  $T_d = 10$  s, 15 s and 20 s, the structure's dynamic behaviors with the frequency  $\nu = 0.5$  Hz are similar and can be divided into three courses:

- (1) At the beginning of deployments, the amplitudes of responses of the structure remain steady, which are exemplified by Fig. 22(a).
- (2) In the middle of deployments, the amplitudes of responses increase, showing the signs of resonance, which are exemplified by Fig. 22(b).
- (3) Near the end of deployments, the structure inclines towards the positive  $x$  direction before collapsing. Additionally, one or more cables can go slack at this time. These are exemplified by Fig. 22(c), where two cables are slack.

For  $T_d = 5$  s, the behavior is a bit different: the structure collapses later at 16 seconds after, instead of during, the deployment. This can be explained by the shorter duration of resonance, which nonetheless has long-term effects on the structure.

Therefore, these results agree well with the prediction about resonance, and thereby demonstrate the proposed approach's abilities to model general tensegrity structure and perform difficult dynamic analyses involving deployments, dynamic environments, and slack cables.

## 7. Conclusion

In this paper, a unified framework based exclusively on non-minimal coordinates (i.e. natural coordinates) is developed for dynamic analysis of tensegrity structures with arbitrary rigid bodies and rigid bars. By doing so, the singularity and ill-definedness problems in minimal formulations of rigid bars are avoided, and the advantages of non-minimal formulations are retained in the system's dynamics. Namely, the resulting dynamic equation has a constant mass matrix and is free from trigonometric functions as well as centrifugal and Coriolis terms.

The natural coordinates are comprehensively reformed. Four, three, and two types of natural coordinates are derived for a 3D rigid body, a 2D rigid body, and a 3D or 2D rigid bar. Different types of natural coordinates represent different arrangements of basic points and base vectors, and hence give much flexibility to model joints between rigid bodies or between rigid bodies and rigid bars. These different types of coordinates are then abstracted and unified into a universal transformation relation (16). By employing the idea of polymorphism, not only mathematical expressions are simplified in the derivations of dynamics but also generic computer codes are made easy.

Solution methods are also developed to enable extensive analyses of tensegrity structures under the same framework. Static analysis methods are for-

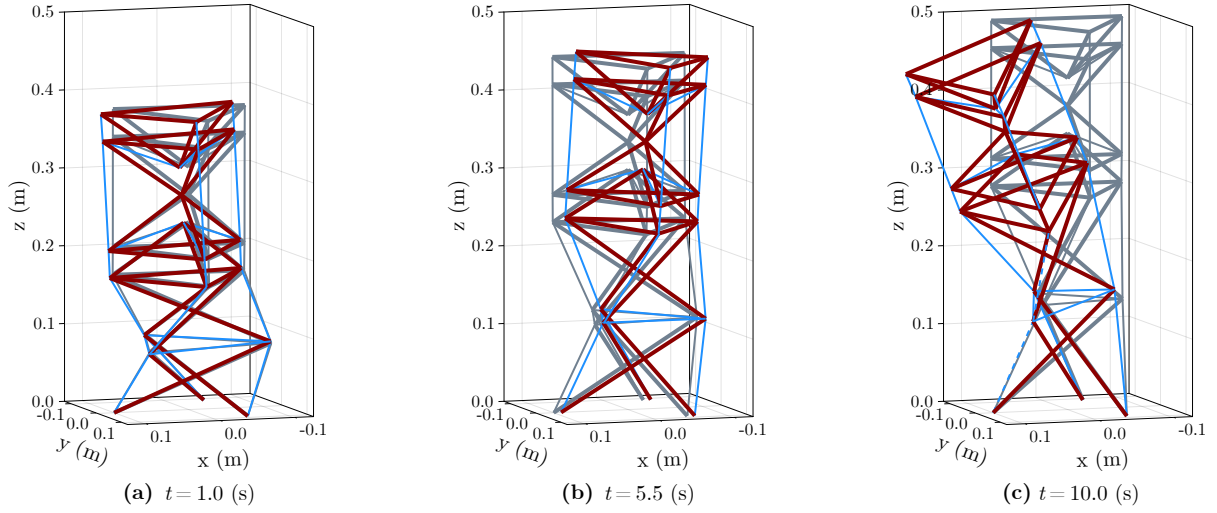


Figure 22: Snapshots at times (a)  $t = 1.0$  s, (b)  $t = 5.5$  s, and (c)  $t = 10$  s of the 3D tensegrity structure deploying with a seismic frequency  $\nu = 0.5$  Hz and a deployment duration  $T_d = 10$  s.

ulated to determine the static equilibrium states of tensegrity configurations. Using the Lagrange-d'Alembert principle, a set of DAEs is derived for the nonlinear dynamics of tensegrity systems. Numerical analysis of constrained nonlinear dynamics is enabled by deriving a symplectic integration scheme with modifications adapted to non-conservative forces and boundary conditions. Modal analysis is also enabled by linearizing the governing DAEs around static equilibrium and using the reduced-basis method, so that the inherent dynamic characteristics, such as natural frequencies and mode shapes, can be easily calculated.

The proposed approach is comprehensively verified by comparing against reference results when possible. In particular, numerical integration solutions are very close to those from minimal formulations, even when a much larger timestep is used. The maximum relative error of natural frequencies between the proposed approach and the commercial software Adams is  $4 \times 10^{-9}$ .

Situations, where it is hard to make direct comparisons with reference results, are also investigated. Different constitute laws are considered in the seismic simulations of the 2D tensegrity tower, showing the proposed approach's ability to deal with non-conservative tension forces, including multiple slacking events in the cables. The nonlinear dynamics of a 3D deployable tensegrity structure with 6-DoF rigid bodies and 5-DoF rigid bars is simulated, which is hard if not impossible in most commercial softwares. Simulations of cable-based deployments on a seismic ground under gravity loads also demonstrate the ability to cope with complex conditions that are close to real world.

Furthermore, the two novel designs of tensegrity structures exemplify new ways to integrate Class-1-to- $k$  tensegrity modules with arbitrary rigid bodies and rigid bars to create multi-functional composite structures.

Regarding future research, the proposed framework can be extended to include cable masses [27, 43], which are ignored in this paper, and clustered cables, which slide through pulleys on the rigid members to achieve clustered actuation [21, 49]. These extensions should be straightforward due to the same underlying framework of Lagrangian mechanics. Finally, the linear dependence

on cables' force densities (29) can be exploited for the design of control schemes [11], aiming to integrate structure and control design in the same vein as [50].

#### CRediT author statement

**Jiahui Luo:** Conceptualization, Methodology, Software, Validation, Writing – Original draft. **Zhigang Wu:** Conceptualization, Supervision, Project administration, Writing - Review & Editing. **Xiaoming Xu:** Conceptualization, Methodology, Formal analysis, Supervision, Writing – Review & editing.

#### Declaration of interests

The authors declare that they have no known competing financial interests or personal relationships that could have appeared to influence the work reported in this paper.

#### Acknowledgments

The research work reported in this paper is supported by the National Natural Science Foundation of China under Grants 12002396.

#### Data availability statement

The raw/processed data required to reproduce these findings cannot be shared at this time as the data also forms part of an ongoing study. However, parts of the data can be shared with interested researchers upon request.

#### Appendix A. Mass matrices

Let's introduce a local Cartesian frame  $\bar{O}\bar{x}\bar{y}\bar{z}$  or  $\bar{O}\bar{x}\bar{y}$  which is fixed on the rigid member  $\mathcal{J}$ , as shown in Fig. A.24. Quantities expressed in this local frame are denoted by an overline  $\bar{\cdot}$ . Without loss of generality, let its origin  $\bar{O}$

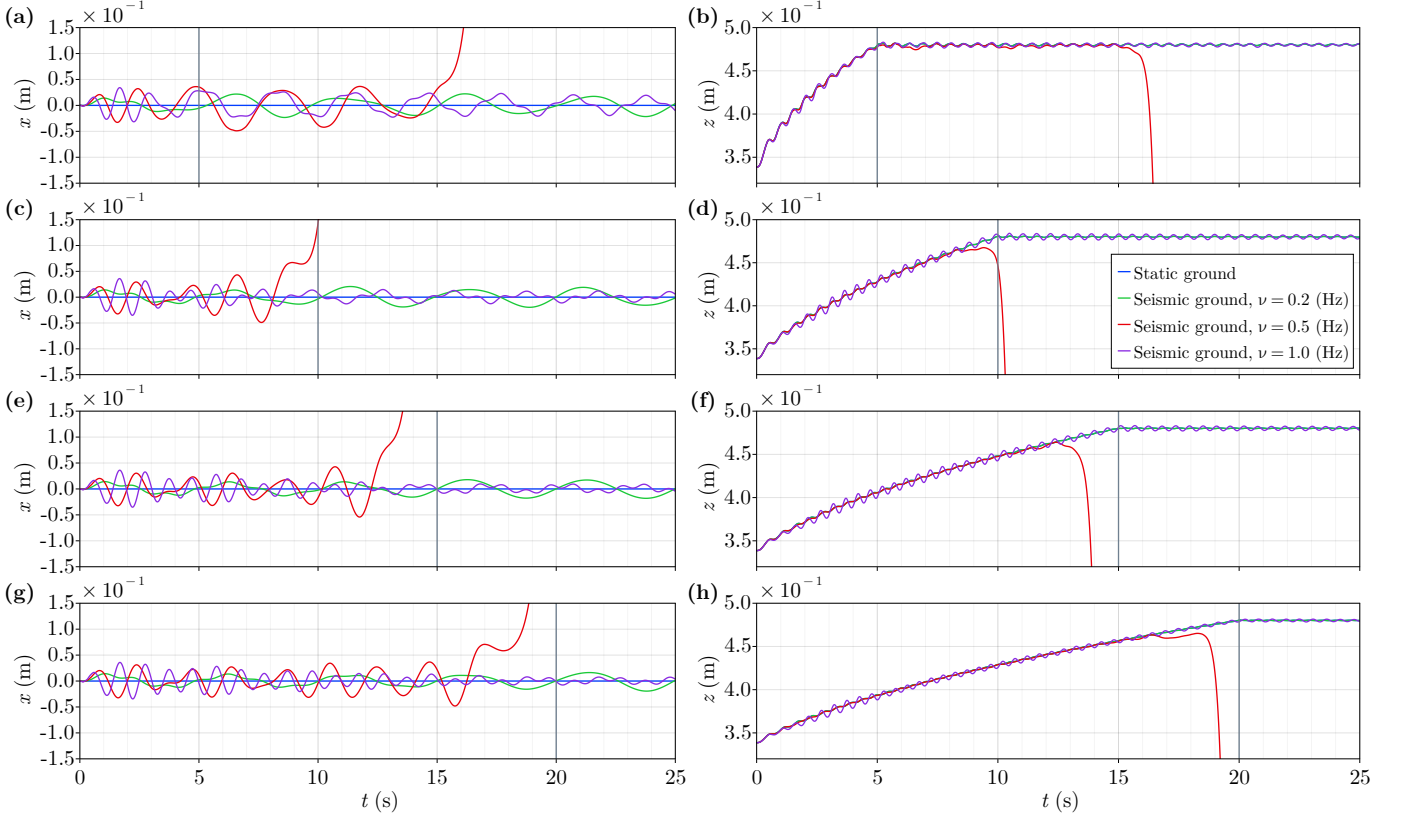


Figure 23: Time histories of the (a,c,e,g)  $x$  and (b,d,f,h)  $z$  coordinates of  $\mathbf{r}_{10,g}$  for the 3D tensegrity structure with deployment durations (a,b)  $T_d = 5$  s, (c,d)  $T_d = 10$  s, (e,f)  $T_d = 15$  s, (g,h)  $T_d = 20$  s.

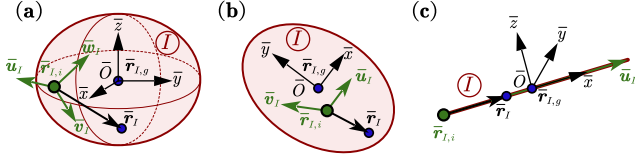


Figure A.24: The basic point  $\bar{\mathbf{r}}_{1,i}$ , the base vectors  $\bar{\mathbf{u}}_i$ ,  $\bar{\mathbf{v}}_i$  and  $\bar{\mathbf{w}}_i$ , the mass center  $\bar{\mathbf{r}}_{1,g}$ , and a generic point  $\bar{\mathbf{r}}_i$  in the local Cartesian frame of a (a) 3D or (b) 2D rigid body or (c) a rigid bar. coincide with the mass center, such that  $\bar{\mathbf{r}}_{1,g} = \mathbf{0}$ . For 3D and 2D rigid bodies, let its axes align along the principal axes of inertia. For a 3D (or 2D) rigid bar, let its  $\bar{x}$  axis aligns along the longitudinal direction.

Because the basic points and base vectors are fixed on the rigid members, their coordinates in the local frame are constant. Let's define a polymorphic matrix  $\bar{\mathbf{X}}_I$  with three definitions

$$\bar{\mathbf{X}}_I = \begin{cases} [\bar{\mathbf{u}}, \bar{\mathbf{v}}, \bar{\mathbf{w}}] & \text{(A.1a)} \\ [\bar{\mathbf{u}}, \bar{\mathbf{v}}] & \text{(A.1b)} \\ [\bar{\mathbf{u}}] & \text{(A.1c)} \end{cases}$$

for the three standard types of natural coordinates  $\bar{\mathbf{q}}_{I,ruvw}$ ,  $\bar{\mathbf{q}}_{I,ruv}$ , and  $\bar{\mathbf{q}}_{I,ru}$ , respectively. Then, according to (14), the position vector of a generic point in the local frame can be expressed by  $\bar{\mathbf{r}} = \bar{\mathbf{r}}_{1,i} + \bar{\mathbf{X}}_I \mathbf{c}_I$ , which gives

$$\mathbf{c}_I = \bar{\mathbf{X}}_I^+ (\bar{\mathbf{r}} - \bar{\mathbf{r}}_{1,i}) \quad (\text{A.2})$$

where  $(\cdot)^+$  denotes the Moore-Penrose pseudoinverse. For (A.1a) and (A.1b), because the columns are linearly independent, i.e.  $\bar{\mathbf{X}}$  has full rank, the pseudoinverse is equal to the matrix inverse.

Using (A.2), the following expressions for use in (18) can be derived:

$$\int_{\Omega} \rho_I d\Omega = m_I \quad (\text{A.3a})$$

$$\int_{\Omega} \rho_I \mathbf{c}_I d\Omega = m_I \bar{\mathbf{X}}^+ (\bar{\mathbf{r}}_{1,g} - \bar{\mathbf{r}}_{1,i}) = -m_I \bar{\mathbf{X}}^+ \bar{\mathbf{r}}_{1,i} \quad (\text{A.3b})$$

$$\int_{\Omega} \rho_I \mathbf{c}_I \mathbf{c}_I^T d\Omega = \bar{\mathbf{X}}^+ (\bar{\mathbf{J}}_I - m_I \bar{\mathbf{r}}_{1,i} \bar{\mathbf{r}}_{1,i}^T - m_I \bar{\mathbf{r}}_{1,g} \bar{\mathbf{r}}_{1,i}^T + m_I \bar{\mathbf{r}}_{1,i} \bar{\mathbf{r}}_{1,i}^T) \bar{\mathbf{X}}^{+T} \quad (\text{A.3c})$$

$$= \bar{\mathbf{X}}^+ (\bar{\mathbf{J}}_I + m_I \bar{\mathbf{r}}_{1,i} \bar{\mathbf{r}}_{1,i}^T) \bar{\mathbf{X}}^{+T} \quad (\text{A.3d})$$

where  $m_I$  is the mass of the rigid member  $\mathcal{I}$ ;  $\bar{\mathbf{J}}_I$  contains the moments of inertia and necessitates some discussions:

For a 3D rigid body, we have

$$\bar{\mathbf{J}}_I = \int_{\Omega} \rho_I \bar{\mathbf{r}} \bar{\mathbf{r}}^T d\Omega = \int_{\Omega} \rho_I \begin{bmatrix} \bar{x}^2 & \bar{y}\bar{x} & \bar{z}\bar{x} \\ \bar{x}\bar{y} & \bar{y}^2 & \bar{z}\bar{y} \\ \bar{x}\bar{z} & \bar{y}\bar{z} & \bar{z}^2 \end{bmatrix} d\Omega \quad (\text{A.4})$$

which is related to the inertia matrix

$$\bar{\mathbf{I}}_I = \int_{\Omega} \rho_I \begin{bmatrix} \bar{y}^2 + \bar{z}^2 & -\bar{y}\bar{x} & -\bar{z}\bar{x} \\ -\bar{x}\bar{y} & \bar{x}^2 + \bar{z}^2 & -\bar{z}\bar{y} \\ -\bar{x}\bar{z} & -\bar{y}\bar{z} & \bar{x}^2 + \bar{y}^2 \end{bmatrix} d\Omega \quad (\text{A.5})$$

$$\text{by } \bar{\mathbf{J}}_I = \frac{1}{2} \text{trace}(\bar{\mathbf{I}}_I) \mathbf{I}_3 - \bar{\mathbf{I}}_I.$$

For a 2D rigid body, we have

$$\bar{\mathbf{J}}_I = \int_{\Omega} \rho_I \bar{\mathbf{r}} \bar{\mathbf{r}}^T d\Omega = \int_{\Omega} \rho_I \begin{bmatrix} \bar{x}^2 & \bar{y}\bar{x} \\ \bar{x}\bar{y} & \bar{y}^2 \end{bmatrix} d\Omega \quad (\text{A.6})$$

which is related to the polar moment of inertia  $I_z = \int_{\Omega} \rho_I (\bar{x}^2 + \bar{y}^2) d\Omega$  by  $I_z = \text{trace}(\bar{J}_I)$ . Note that because the local frame's axes align along the principal axes of inertia, non-diagonal elements of (A.4) to (A.6) are zeros.

For a 3D rigid bar, the expression of  $\bar{J}_I$  is the same as (A.4), except that only the element  $\bar{x}^2$  is nonzero. And the pseudoinverse of  $\bar{X}_I = [\bar{u}_x, 0, 0]^T$  is  $\bar{X}_I^+ = [1/\bar{u}_x, 0, 0]$ . Therefore, we have  $\bar{X}_I^+ \bar{J}_I \bar{X}_I^{+T} = \left( \int_{\Omega} \rho_I \bar{x}^2 d\Omega \right) / \bar{u}_x^2$ .

The mass matrix for a 2D rigid bar is similar.

## Appendix B. Partial derivatives

This appendix derives the partial derivatives of the generalized tension force  $\bar{Q}$  which are needed by the linearized dynamic equation (42) and the Jacobian matrix (55) for the integration scheme. To this end, let's first derive the partial derivatives of  $l_j$ ,  $\hat{l}_j$ , and  $\hat{l}_j$ :

$$\frac{\partial l_j}{\partial \mathbf{q}} = \frac{\mathbf{q}^T \mathbf{U}_j}{l_j} = \hat{l}_j^T \mathbf{J}_j \quad \frac{\partial l_j}{\partial \hat{\mathbf{q}}} = \mathbf{0}^T \quad (\text{B.1a})$$

$$\frac{\partial \hat{l}_j}{\partial \mathbf{q}} = \frac{\mathbf{J}_j - \hat{l}_j \frac{\partial l_j}{\partial \mathbf{q}}}{l_j} = \frac{\mathbf{J}_j - \hat{l}_j \hat{l}_j^T \mathbf{J}_j}{l_j} \quad \frac{\partial \hat{l}_j}{\partial \hat{\mathbf{q}}} = \mathbf{0}^T \quad (\text{B.1b})$$

$$\frac{\partial \hat{l}_j}{\partial \mathbf{q}} = \frac{l_j \mathbf{q}^T - l_j \mathbf{q}^T}{l_j^2} \mathbf{U}_j \quad \frac{\partial \hat{l}_j}{\partial \hat{\mathbf{q}}} = \frac{\mathbf{q}^T \mathbf{U}_j}{l_j} = \hat{l}_j^T \mathbf{J}_j \quad (\text{B.1c})$$

Considering the constitutive law (30), and assume the cables are in tension. Then the partial derivatives of  $f_j$  reads, respectively,

$$\frac{\partial f_j}{\partial \mathbf{q}} = \kappa_j \frac{\partial l_j}{\partial \mathbf{q}} + \eta_j \frac{\partial \hat{l}_j}{\partial \mathbf{q}} \quad \text{and} \quad \frac{\partial f_j}{\partial \hat{\mathbf{q}}} = \eta_j \frac{\partial \hat{l}_j}{\partial \hat{\mathbf{q}}} \quad (\text{B.2})$$

Finally, using (B.1) and (B.2), the partial derivatives of  $\bar{Q}$  can be derived by, respectively,

$$\begin{aligned} \frac{\partial \bar{Q}}{\partial \mathbf{q}} &= \frac{\partial \bar{Q}}{\partial \mathbf{q}} \dot{\mathbf{E}} = -\dot{\mathbf{E}}^T \mathbf{J}_j^T \frac{\partial f_j}{\partial \mathbf{q}} \dot{\mathbf{E}} = -\dot{\mathbf{E}}^T \mathbf{J}_j^T \left( \hat{l}_j \frac{\partial f_j}{\partial \mathbf{q}} + f_j \frac{\partial \hat{l}_j}{\partial \mathbf{q}} \right) \dot{\mathbf{E}} \\ &= -\dot{\mathbf{E}}^T \mathbf{J}_j^T \left( \hat{l}_j \left( \kappa_j \hat{l}_j^T \mathbf{J}_j + \eta_j \left( \frac{l_j \mathbf{q}^T - l_j \mathbf{q}^T}{l_j^2} \right) \mathbf{U}_j \right) + f_j \frac{\mathbf{J}_j - \hat{l}_j \hat{l}_j^T \mathbf{J}_j}{l_j} \right) \dot{\mathbf{E}} \\ &= -\dot{\mathbf{E}}^T \left( \mathbf{J}_j^T (\beta_j \mathbf{I}_3 + (\kappa_j - \beta_j) \hat{l}_j \hat{l}_j^T) \mathbf{J}_j \right) \dot{\mathbf{E}} \end{aligned} \quad (\text{B.3})$$

and

$$\begin{aligned} \frac{\partial \bar{Q}}{\partial \hat{\mathbf{q}}} &= \frac{\partial \bar{Q}}{\partial \hat{\mathbf{q}}} \dot{\mathbf{E}} = -\dot{\mathbf{E}}^T \mathbf{J}_j^T \frac{\partial f_j}{\partial \hat{\mathbf{q}}} \dot{\mathbf{E}} = -\dot{\mathbf{E}}^T \mathbf{J}_j^T \left( \hat{l}_j \frac{\partial f_j}{\partial \hat{\mathbf{q}}} + f_j \frac{\partial \hat{l}_j}{\partial \hat{\mathbf{q}}} \right) \dot{\mathbf{E}} \\ &= -\dot{\mathbf{E}}^T \left( \eta_j \mathbf{J}_j^T \hat{l}_j \hat{l}_j^T \mathbf{J}_j \right) \dot{\mathbf{E}} \end{aligned} \quad (\text{B.4})$$

where  $\beta_j = \eta_j \hat{l}_j / l_j + \gamma_j$ . When a cable is slack, its tension force's partial derivations are set to zeros.

## References

[1] F. R. Buckminster, Tensile-integrity structures (Nov. 1962).  
[2] H. Lalvani, Origins Of Tensegrity: Views Of Emmerich, Fuller And Snelson, International Journal of Space Structures 11 (1-2) (1996) 27–27.  
[3] R. E. Skelton, M. C. de Oliveira, Tensegrity Systems, Springer, Dordrecht ; New York, 2009.  
[4] H. Furuya, Concept of Deployable Tensegrity Structures in Space Application, International Journal of Space Structures 7 (2) (1992) 143–151.

[5] C. Sultan, R. Skelton, Deployment of tensegrity structures, International Journal of Solids and Structures 40 (18) (2003) 4637–4657.  
[6] S. Krishnan, B. Li, Design of Lightweight Deployable Antennas Using the Tensegrity Principle, in: Earth and Space 2018, American Society of Civil Engineers, Cleveland, Ohio, 2018, pp. 888–899.  
[7] C. Sultan, Chapter 2 Tensegrity: 60 Years of Art, Science, and Engineering, in: Advances in Applied Mechanics, Vol. 43 of Advances in Applied Mechanics, Elsevier, 2009, pp. 69–145.  
[8] A. C. Sychterz, I. F. C. Smith, Using dynamic measurements to detect and locate ruptured cables on a tensegrity structure, Engineering Structures 173 (2018) 631–642.  
[9] N. Veuve, S. D. Safaei, I. F. C. Smith, Deployment of a Tensegrity Footbridge, Journal of Structural Engineering 141 (11) (2015) 04015021.  
[10] A. G. Tibert, S. Pellegrino, Deployable Tensegrity Reflectors for Small Satellites, Journal of Spacecraft and Rockets 39 (5) (2002) 701–709.  
[11] M. Chen, J. Liu, R. E. Skelton, Design and control of tensegrity morphing airfoils, Mechanics Research Communications 103 (2020) 103480.  
[12] M. Chen, R. Goyal, M. Majji, R. E. Skelton, Design and analysis of a growable artificial gravity space habitat, Aerospace Science and Technology 106 (2020) 106147.  
[13] K. Snelson, The Art of Tensegrity, International Journal of Space Structures 27 (2-3) (2012) 71–80.  
[14] S. M. Levin, THE TENSEGRITY-TRUSS AS A MODEL FOR SPINE MECHANICS: BIOTENSEGRITY, Journal of Mechanics in Medicine and Biology 02 (03n04) (2002) 375–388.  
[15] S. Lessard, J. Bruce, E. Jung, M. Teodorescu, V. SunSpiral, A. Agogino, A lightweight, multi-axis compliant tensegrity joint, in: 2016 IEEE International Conference on Robotics and Automation (ICRA), IEEE, Stockholm, Sweden, 2016, pp. 630–635.  
[16] B. Chen, H. Jiang, Swimming Performance of a Tensegrity Robotic Fish, Soft Robotics 6 (4) (2019) 520–531.  
[17] S. Liu, Q. Li, P. Wang, F. Guo, Kinematic and static analysis of a novel tensegrity robot, Mechanism and Machine Theory 149 (2020) 103788.  
[18] Y. Wang, X. Xu, Y. Luo, Topology design of general tensegrity with rigid bodies, International Journal of Solids and Structures 202 (2020) 278–298.  
[19] A. Wroldsen, M. de Oliveira, R. Skelton, Modelling and control of non-minimal non-linear realisations of tensegrity systems, International Journal of Control 82 (3) (2009) 389–407.  
[20] Z. Kan, H. Peng, B. Chen, W. Zhong, A sliding cable element of multibody dynamics with application to nonlinear dynamic deployment analysis of clustered tensegrity, International Journal of Solids and Structures 130–131 (2018) 61–79.  
[21] Z. Kan, N. Song, H. Peng, B. Chen, X. Song, A comprehensive framework for multibody system analysis with clustered cables: Examples of tensegrity structures, International Journal of Solids and Structures 210–211 (2021) 289–309.  
[22] M. Cefalo, J. M. Mirats-Tur, A comprehensive dynamic model for class-I tensegrity systems based on quaternions, International Journal of Solids and Structures 48 (5) (2011) 785–802.  
[23] R. Skelton, Dynamics and Control of Tensegrity Systems, in: G. Gladwell, H. Ulbrich, W. Günthner (Eds.), IUTAM Symposium on Vibration Control of Non-linear Mechanisms and Structures, Vol. 130, Springer Netherlands, Dordrecht, 2005, pp. 309–318.

- [24] R. E. Skelton, Efficient Models of Multi-body Dynamics, in: R. Blockley, W. Shyy (Eds.), *Encyclopedia of Aerospace Engineering*, John Wiley & Sons, Ltd, Chichester, UK, 2010, p. eae301.
- [25] K. Nagase, R. E. Skelton, Network and vector forms of tensegrity system dynamics, *Mechanics Research Communications* 59 (2014) 14–25.
- [26] J. Cheong, R. E. Skelton, Nonminimal Dynamics of General Class k Tensegrity Systems, *International Journal of Structural Stability and Dynamics* 15 (02) (2015) 1450042.
- [27] R. Goyal, R. E. Skelton, Tensegrity system dynamics with rigid bars and massive strings, *Multibody System Dynamics* 46 (3) (2019) 203–228.
- [28] S.-C. Hsu, V. Tadiparthi, R. Bhattacharya, A Lagrangian method for constrained dynamics in tensegrity systems with compressible bars, *Computational Mechanics* 67 (1) (2021) 139–165.
- [29] S. Ma, M. Chen, Z. Peng, X. Yuan, R. Skelton, The Equilibrium and Form-Finding of General Tensegrity Systems with Rigid Bodies, *Engineering Structures* (2022).
- [30] X. M. Xu, J. H. Luo, X. G. Feng, H. J. Peng, Z. G. Wu, A generalized inertia representation for rigid multibody systems in terms of natural coordinates, *Mechanism and Machine Theory* 157 (2021) 104174.
- [31] J. G. De Jalón, J. Unda, A. Avello, Natural coordinates for the computer analysis of multibody systems, *Computer Methods in Applied Mechanics and Engineering* 56 (3) (1986) 309–327.
- [32] J. García de Jalón, J. Unda, A. Avello, J. M. Jiménez, Dynamic Analysis of Three-Dimensional Mechanisms in “Natural” Coordinates, *Journal of Mechanisms, Transmissions, and Automation in Design* 109 (4) (1987) 460–465.
- [33] J. G. de Jalón, Twenty-five years of natural coordinates, *Multibody System Dynamics* 18 (1) (2007) 15–33.
- [34] J. G. De Jalon, E. Bayo, *Kinematic and Dynamic Simulation of Multibody Systems: The Real-Time Challenge*, Mechanical Engineering Series, Springer-Verlag, New York, 1994.
- [35] C. M. Pappalardo, A natural absolute coordinate formulation for the kinematic and dynamic analysis of rigid multibody systems, *Nonlinear Dynamics* 81 (4) (2015) 1841–1869.
- [36] V. Böhm, I. Zeidis, K. Zimmermann, An approach to the dynamics and control of a planar tensegrity structure with application in locomotion systems, *International Journal of Dynamics and Control* 3 (1) (2015) 41–49.
- [37] J. Luo, Z. Wu, X. Xu, Y. Chen, Z. Liu, L. Ming, Forward Statics of Tensegrity Robots With Rigid Bodies Using Homotopy Continuation, *IEEE Robotics and Automation Letters* 7 (2) (2022) 5183–5190.
- [38] M. Arnold, O. Brüls, Convergence of the generalized- $\alpha$  scheme for constrained mechanical systems, *Multibody System Dynamics* 18 (2) (2007) 185–202.
- [39] W. X. Zhong, Q. Gao, Integration of constrained dynamical system via analytical structural mechanics, *Journal of Dynamics and Control* 4 (3) (2006) 193–200.
- [40] F. Wu, W. Zhong, Constrained Hamilton variational principle for shallow water problems and Zu-class symplectic algorithm, *Applied Mathematics and Mechanics* 37 (1) (2016) 1–14.
- [41] K. Yildiz, G. A. Lesieutre, Sizing and prestress optimization of Class-2 tensegrity structures for space boom applications, *Engineering with Computers* (Jul. 2020).
- [42] O. A. Bauchau, A. Epple, C. L. Bottasso, Scaling of Constraints and Augmented Lagrangian Formulations in Multibody Dynamics Simulations, *Journal of Computational and Nonlinear Dynamics* 4 (021007) (Mar. 2009).
- [43] Z. Kan, H. Peng, B. Chen, W. Zhong, Nonlinear dynamic and deployment analysis of clustered tensegrity structures using a positional formulation FEM, *Composite Structures* 187 (2018) 241–258.
- [44] N. Ashweari, A. Eriksson, Natural frequencies describe the pre-stress in tensegrity structures, *Computers & Structures* 138 (2014) 162–171.
- [45] W. Zhao, A. Pashkevich, A. Klimchik, D. Chablat, Elastostatic Modeling of Multi-Link Flexible Manipulator Based on Two-Dimensional Dual-Triangle Tensegrity Mechanism, *Journal of Mechanisms and Robotics* 14 (2) (2022) 021002.
- [46] B. R. Tietz, R. W. Carnahan, R. J. Bachmann, R. D. Quinn, V. SunSpiral, Tetraspine: Robust terrain handling on a tensegrity robot using central pattern generators, in: 2013 IEEE/ASME International Conference on Advanced Intelligent Mechatronics, IEEE, Wollongong, NSW, 2013, pp. 261–267.
- [47] K. M. Roffman, G. A. Lesieutre, Cable-Actuated Articulated Cylindrical Tensegrity Booms, in: AIAA Scitech 2019 Forum, AIAA SciTech Forum, American Institute of Aeronautics and Astronautics, 2019.
- [48] N. Bel Hadj Ali, L. Rhode-Barbarigos, I. F. C. Smith, Analysis of clustered tensegrity structures using a modified dynamic relaxation algorithm, *International Journal of Solids and Structures* 48 (5) (2011) 637–647.
- [49] S. Ma, M. Chen, R. E. Skelton, Dynamics and control of clustered tensegrity systems, *Engineering Structures* 264 (2022) 114391.
- [50] R. Goyal, M. Majji, R. E. Skelton, Integrating structure, information architecture and control design: Application to tensegrity systems, *Mechanical Systems and Signal Processing* 161 (2021) 107913.